Chem Soc Rev

Cite this: *Chem. Soc. Rev.*, 2011, **40**, 4167–4185

www.rsc.org/csr

CRITICAL REVIEW

Nanomaterials of high surface energy with exceptional properties in catalysis and energy storage

Zhi-You Zhou, Na Tian, Jun-Tao Li, Ian Broadwell and Shi-Gang Sun*

Received 10th November 2010
DOI: 10.1039/c0cs00176g

The properties of nanomaterials for use in catalytic and energy storage applications strongly depends on the nature of their surfaces. Nanocrystals with high surface energy have an open surface structure and possess a high density of low-coordinated step and kink atoms. Possession of such features can lead to exceptional catalytic properties. The current barrier for widespread industrial use is found in the difficulty to synthesise nanocrystals with high-energy surfaces. In this *critical review* we present a review of the progress made for producing shape-controlled synthesis of nanomaterials of high surface energy using electrochemical and wet chemistry techniques. Important nanomaterials such as nanocrystal catalysts based on Pt, Pd, Au and Fe, metal oxides TiO_2 and SnO_2, as well as lithium Mn-rich metal oxides are covered. Emphasis of current applications in electrocatalysis, photocatalysis, gas sensor and lithium ion batteries are extensively discussed. Finally, a future synopsis about emerging applications is given (139 references).

1. Introduction

Nanomaterials are of immense importance in today's modern society. The development of chemical industries, environmental protection and new-energy resources (*e.g.*, fuel cells, lithium ion batteries) have long relied on nanomaterials with exceptional properties. The fields of catalysis, electrocatalysis, photocatalysis and photoelectricity are all examples of where nanotechnology is impacting on current science.[1–4] As particle dimensions reduce towards the nanoscale, the surface-to-volume ratio proportionally increases and small-size effects associated with nanoparticles become more pronounced. Understanding the nanoscale topography of surface sites, such as terraces, steps, kinks, adatoms and vacancies, and their effects on catalytic and other physico-chemical properties is the key to designing nanoscale functional materials by nanotechnology.[5–7]

The performance of nanocrystals used as catalysts depends strongly on the surface structure of facets enclosing the crystals. Thermodynamics usually ensures that crystal facets evolve to have the lowest surface energy during the crystal growth process. For a pure metal, the surface energy relies on coordination numbers (CNs) of surface atoms as well as their density. For example, it increases in the order of $\gamma_{\{111\}} < \gamma_{\{100\}} < \gamma_{\{110\}} < \gamma_{\{hkl\}}$ on a face-centered cubic (fcc) metal, where

State Key Laboratory of Physical Chemistry of Solid Surfaces, Department of Chemistry, College of Chemistry and Chemical Engineering, School of Energy Research, Xiamen University, Xiamen 361005, China. E-mail: sgsun@xmu.edu.cn; Fax: +86 0592 2183047

Zhi-You Zhou

Zhi-You Zhou received his PhD degree in 2004 from Xiamen University. He is an associate professor at the Department of Chemistry of Xiamen University and his research interests include electrochemical in situ FTIRS, electrocatalysis, fuel cells and nanomaterials.

Na Tian

Na Tian received her PhD degree in 2007 from Xiamen University. She is an associate professor at the Department of Chemistry of Xiamen University and her research interests focus on electrocatalysis and nanomaterials.

{*hkl*} represents high-index planes with at least one Miller index larger than 1.[8,9] For a metal oxide, the surface energy increases with increasing density of dangling bonds. Generally, high-energy surfaces have an open surface structure and possess exceptional properties. Long-term fundamental studies in surface science have shown that Pt high-index planes with open surface structure exhibit much higher reactivity than that of (111) or (100) low-index planes, because high-index planes have a large density of low-coordinated atoms situated on steps and kinks, with high reactivity required for high catalytic activity.[10–12] More importantly, on high-index planes, there exist short-range steric sites (such as "chair" sites) that are considered as active sites and consist of the combination of several (typical 5–6) step and terrace atoms.[13,14] Due to synergistic effect between step and terrace atoms, steric sites usually serve as catalytically active sites. Besides, open-structure surfaces also play a very important role in the charging/discharging process of lithium ion batteries. They can provide parallel channels, where Li^+ ions are able to intercalate through the surface with the least resistance compared to other crystal plane orientations.[15] This favors fast ion transfer between surface and interior.

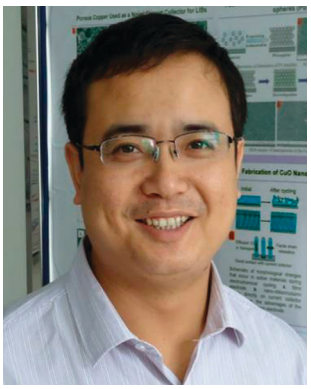

Jun-Tao Li

Jun-Tao Li received his PhD degree in 2009 from Xiamen University and University of Pierre et Marie Curie. He currently works in Energy Research School, Xiamen University, focusing on electrochemical conversion and storage systems.

Normally, nanocrystals with low surface energy such as those formed under normal conditions usually have low catalytic activities. Those with high surface energies are known to possess enhanced catalytic properties. The goal here is to create nanocrystal catalysts which have high surface energy facets. Unfortunately, this presents a big challenging. When a crystal grows, different facets grow with different rates. High-energy facets typically have higher growth rates than low-energy facets. Overall, the final crystal shape is dominated by the slow-growth facets that have low surface energy.[16] Taking Pt as an example, after the pioneering work of El-Sayed and co-workers who synthesized cubic and tetrahedral Pt nanocrystals through chemical reduction of K_2PtCl_4 by H_2 in the presence of polyacrylate in 1996,[17] various Pt nanocrystals with different shapes have been obtained by changing Pt precursors, reducing agents, stabilizing reagents and solvents.[18–26] Nevertheless, the surface structure of the synthesized Pt nanoparticles is limited to low-index facets of {111} and {100}, and few Pt nanocrystals with high-index facets are produced by conventional wet chemistry synthesis.[27–29] Remarkably, substantial progress has been made in overcoming the obstacle to form nanocrystals with high-energy facets in recent years.[30–32]

Although there are several excellent reviews about shape-controlled synthesis of metal nanocrystals, they mainly describe nanocrystals with low-energy facets.[28,33,34] In this review, after a brief introduction of the relationship between surface structure and crystal shapes, we focus on the recent progress made in shape-controlled synthesis of metal nanocrystals with high-energy facets and open surface structure, including high-index facets and {110} facets, especially electrochemically shape-controlled synthesis of Pt-group metal nanocrystals. We then describe the synthesis of metal oxide nanomaterials (TiO_2, SnO_2, $Li[Li_{1/3-2x/3}M_xMn_{2/3-x/3}]O_2$, *etc.*) with exposed high-energy surfaces and their unique properties in photocatalysis, gas sensors and Li ion batteries. We finish by considering the challenging issues faced and future perspectives along this exciting new avenue of research.

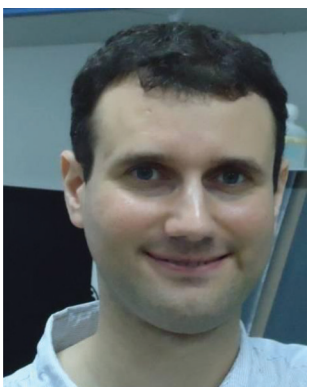

Ian Broadwell

Ian Broadwell received his PhD degree in 2003 from Hull University. Currently he works as EU Science and Technology and post-doctoral Fellow at Xiamen University. His research interests include biomedical application of nanoparticles; microfluidics for biofuel cells and the instrumentation used in biophysics.

Shi-Gang Sun

Shi-Gang Sun received his Doctorat d'Etat in 1986 from Université Pierre et Marie Curie and did one year Post-Doctoral research in the Laboratoire d'Electrochimie Interfacial du CNRS, France. He is presently professor of Chemistry in Xiamen University. His research interests consist of: (1) Electrocatalysis and electrochemical surface science; (2) in situ FTIR spectroscopy; (3) Nanomaterials and chemical power sources. He is president-elect of the Chinese Society of Electrochemistry, Fellow of Royal Society of Chemistry (UK) and Fellow of International Society of Electrochemistry.

2. Relationship between surface structure and crystal shape

For fcc metals (such as Pt, Pd and Au), a unit stereographic triangle (Fig. 1) is often used to illustrate the coordinates of different crystal planes.[14,35] Three vertexes in the triangle represent three low-index planes, *i.e.*, (111), (100) and (110). Other planes lying in the sidelines and inside the triangle are high-index planes. The three sidelines represent [001], [01$\bar{1}$] and [1$\bar{1}$0] crystallographic zones, and corresponding Miller indices can be expressed as {*hk*0}, {*hkk*} and {*hhl*}} ($h \neq k \neq l \neq 0$). The planes inside the triangle can be expressed as {*hkl*}. Fig. 1 also illustrates atomic arrangement models of several typical planes. Clearly, atomic arrangements are highly correlative with Miller indices. The (111) and (100) planes are atomically flat with closely packed surface atoms, and the CNs of surface atoms are 9 and 8, respectively. The (110) plane and high-index planes have open surface structure with low-coordinated step or kink atoms. Step atoms on {*hkk*}, {*hhl*} and (110) planes have the same CNs of 7, while kink atoms on {*hk*0} and {*hkl*} planes have the lowest CNs of 6. Generally, those surfaces possessing a high density of atoms with CNs of 6 and 7 have very high reactivity.

By analogy with the unit stereographic triangle for crystal planes, there is a triangle of polyhedral nanocrystals bounded by corresponding crystal planes (Fig. 2).[14,36] The shapes of nanocrystals situated at the three vertexes are octahedron with {111}, cube with {100} and rhombic dodecahedron with {110}. The polyhedral nanocrystals lying in three sidelines of the triangle are polyhedra bounded by 24 high-index facets: tetrahexahedra (THH) by {*hk*0}, trapezohedra by {*hkk*} and trisoctahedra by {*hhl*}. The polyhedra inside the triangle are hexoctahedra bounded by 48 {*hkl*} facets. Clearly, the polyhedra bounded by high-index facets have unconventional and complex shapes. For identifying them quickly, THH can be considered as a cube with each face capped by a square pyramid; trisoctahedron can be thought as an octahedron with each face capped by a trigonal pyramid, and so on.

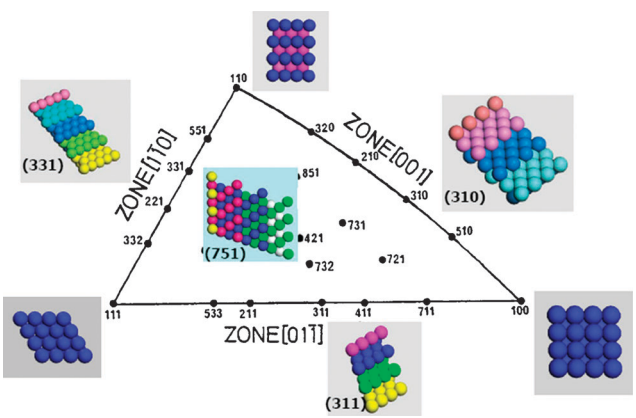

Fig. 1 Unit stereographic triangle of fcc metal single-crystal and models of surface atomic arrangement (modified with permission from ref. 14, copyright 2008, American Chemical Society).

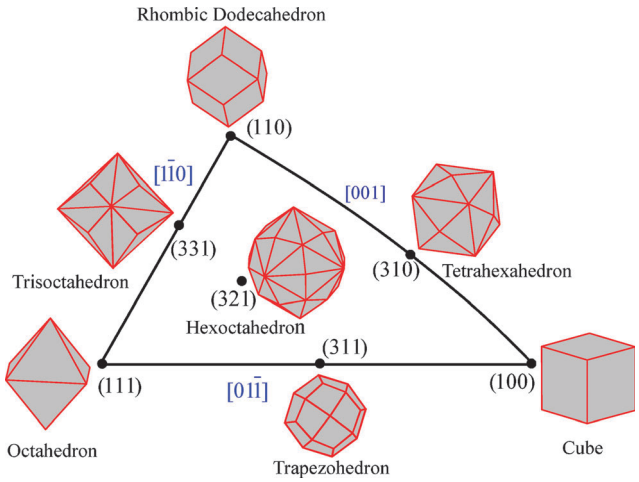

Fig. 2 Unit stereographic triangle of polyhedral nanocrystals bounded by different crystal planes (modified with permission from ref. 14, copyright 2008, American Chemical Society).

3. Shape-controlled synthesis of metal nanocrystals of high surface energy and open surface structure

We focus, in this section, on the progress made in shape-controlled synthesis of metal nanocrystals of high surface energy and open surface structure, *i.e.* high-index facets and {110} facets for fcc metals (Pt, Pd and Au) and {100} for Fe (bcc lattice). To synthesize nanocrystals of high surface energy, we need to develop new synthesis methods that can overcome the thermodynamics limitation, which results in a minimization of the total surface energy of nanocrystals during their growth. Using a surface-structure mediator (such as surfactant, oxygen and halide) that can selectively adsorb or stabilize the high-energy surfaces is one strategy, while another strategy is the more precise electrochemical method which has been developed recently by our group to synthesize metal nanocrystals of high surface energy.

3.1 Pt

Pt nanocrystals due to their excellent activity and stability are widely used and are indispensible catalysts in fuel cells, automotive catalytic converters and petrochemical reforming.[37–40] As Pt is very rare, a key issue is how to improve the intrinsic catalytic properties and utilization efficiency. Shape-controlled synthesis of Pt nanocrystals (NCs) with high-index facets offers a good approach for creating Pt nanocatalyst materials with much higher activities than currently available with commercial Pt catalyst.

As mentioned, the synthesis of Pt nanocrystals with high-index facets is challenging. Conventional electrodeposition of metal nanocrystals made at a constant potential/current in plating solution only yields {111} and {100} low-index facets. Tian *et al.* in 2007 made a breakthrough in synthesis of Pt nanocrystals enclosed with high-index facets by developing an electrochemical method.[30] As shown in Fig. 3a, they used a two-step synthesis process. The first step is electrodeposition of polycrystalline Pt nanospheres ~750 nm in diameter on a glassy carbon (GC) electrode. After pre-deposition, a

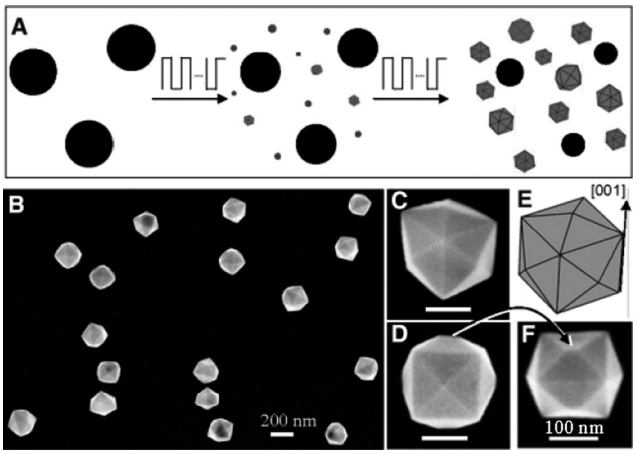

Fig. 3 (A) Scheme of preparation of THH Pt NCs from nanospheres by electrochemical square-wave method. (B) Low-magnification and (C, D, F) high-magnification SEM images of THH Pt NCs. (E) Geometrical model of an ideal THH (modified with permission from ref. 30, copyright 2007, American Association for the Advancement of Science).

square-wave potential was applied to the Pt nanospheres in a solution containing 0.1 M H_2SO_4 + 30 mM ascorbic acid for 5–60 min. The lower (E_L) and upper (E_U) potential limits were *ca.* −0.10 and 1.20 V *vs.* saturated calomel electrode (SCE), respectively, and f = 10 Hz. Under this condition, the Pt nanospheres are partially dissolved at the E_U, and provide low-concentrated Pt ions for the growth of new nanocrystals at the E_L. Interestingly, nearly all of the growing Pt nanocrystals on the GC surface are tetrahexahedral Pt nanocrystals (THH Pt NCs). As shown in Fig. 3b–d, SEM images of the as-prepared Pt nanocrystals show good agreement with a geometrical model of THH (Fig. 3e). The average sizes of the THH Pt NCs can be changed from 20 to 220 nm by controlling the growth time, and the size distribution is relatively narrow, with relative standard deviation (RSD) ranging from 10% to 15%.

Miller indices of exposed surfaces on the THH Pt NCs were identified as mainly {730} facets through the measurement of plane angles between two adjacent facets parallel to the [001] zone axis in a TEM image, as demonstrated in Fig. 4a–c. The Pt(730) plane is periodically composed of two (210) microfacets followed by one (310) microfacet (Fig. 4d), and has a density of step atoms as high as 5.1×10^{14} cm^{-2} (*i.e.* 43% of surface atoms are step atoms). More importantly, all surface atoms on the THH Pt NCs are arranged in such a way that they form active sites for catalysis. Therefore, THH Pt NCs exhibit high catalytic activity. It has been demonstrated that for formic acid electrooxidation, the catalytic activity of THH Pt NCs is 1.6–4.0 times higher than that of polycrystalline Pt nanospheres, and 2.0–3.1 times larger than that of commercial Pt/C catalyst from *E*-TEK Co., Ltd. (Fig. 5a and b). For ethanol electrooxidation, the enhancement factor of the catalytic activity obtained on the THH Pt NCs varies from 2.0 to 4.3 relative to that of Pt nanospheres, and 2.5 to 4.6 relative to commercial Pt/C catalyst (Fig. 5c and d). The THH Pt NCs also exhibit much higher catalytic activity for NO electroreduction than polycrystalline Pt nanoparticles and

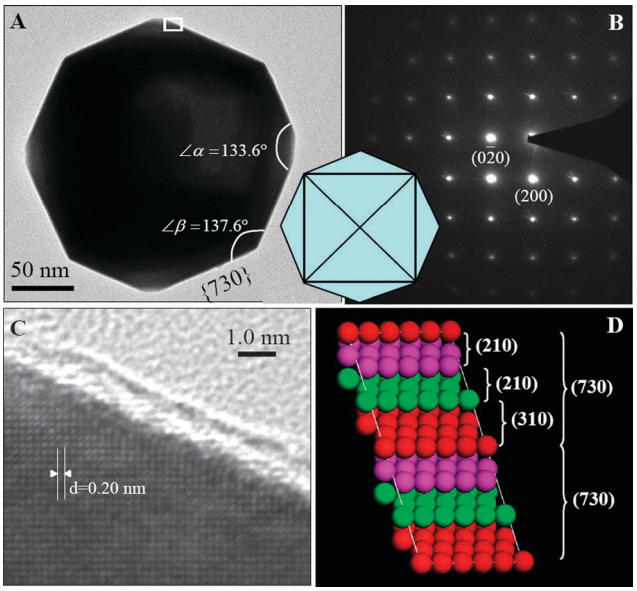

Fig. 4 (A) TEM image and (B) SAED of THH Pt NC recorded along the [001] direction. (C) High-resolution TEM image recorded from the boxed area marked in (A). (D) Atomic model of Pt(730) plane with a high density of stepped surface atoms (modified with permission from ref. 30, copyright 2007, American Association for the Advancement of Science).

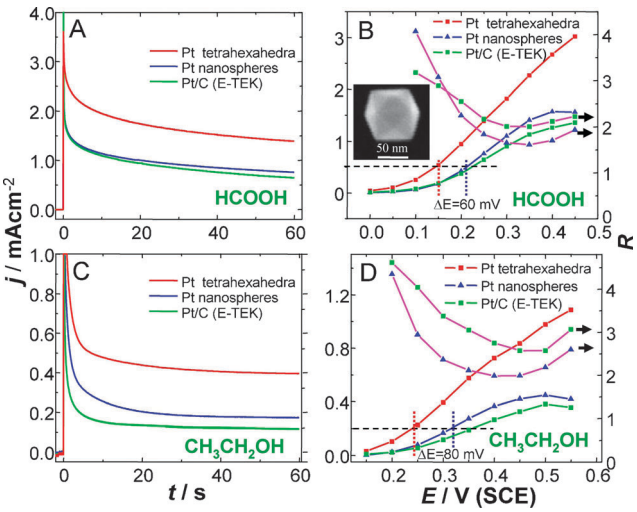

Fig. 5 Comparison of specific catalytic activity among THH Pt NCs, polycrystalline Pt nanospheres and 3.2 nm Pt/C catalyst. (A) Transient current curves recorded at 0.25 V and (B) steady-state current as a function of electrode potential for formic acid electrooxidation in 0.25 M HCOOH + 0.5 M H_2SO_4. (C) Transient current curves recorded at 0.30 V and (D) steady-state current as a function of electrode potential for ethanol electrooxidation in 0.1 M CH_3CH_2OH + 0.1 M $HClO_4$ (modified with permission from ref. 30, copyright 2007, American Association for the Advancement of Science).

bulk Pt electrode.[41] Besides, the high-energy surfaces on the THH Pt NCs are thermally stable up to 815 °C, which is consistent with the theoretical prediction.[42,43]

One important question raised is why high-index facets can form under such electrochemical conditions. The presence of

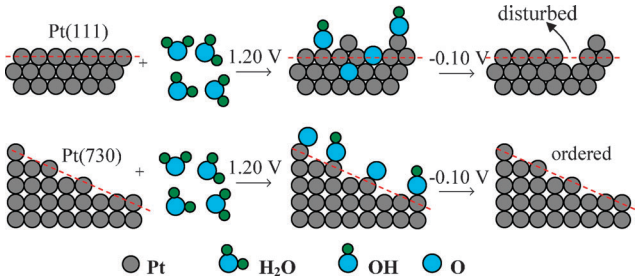

Fig. 6 Schematic illustration of different effects of oxygen adsorption/desorption on Pt(111) and Pt(730). The red dashed line indicates the first layer atoms on the surface (modified with permission from ref. 30, copyright 2007, American Association for the Advancement of Science).

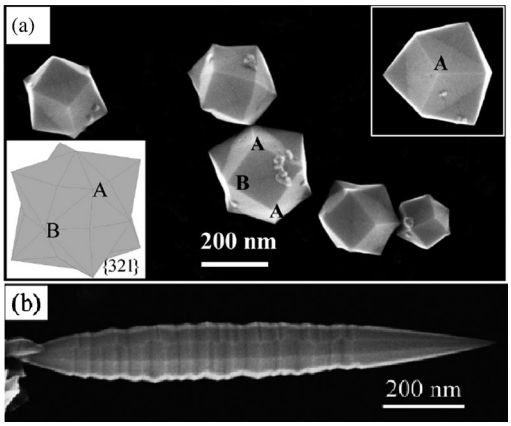

Fig. 7 (a) SEM images of concave hexoctahedral Pt NCs with facets prepared by electrochemical square-wave potential method. The left-lower inset illustrates a model of concave hexoctahedron bounded by {321} facets; (b) SEM images of fivefold twinned Pt nanorods with {*hk*0} high-index facets. The left end is rooted on the original nanosphere (modified with permission from ref. 52, copyright 2008, Royal Society of Chemistry).

ascorbic acid can be excluded, since THH Pt NCs with slightly imperfect shape can still be harvested in ascorbic acid-free solution. Compared with conventional synthesis of metal nanocrystals that only occurs in a reducing environment, the electrochemical square-wave potential method has one unique characteristic. That is, it can cause periodic adsorption/desorption of hydrogen and oxygen on metal surfaces, as well as nucleation and growth/dissolution of the metals.[30,44] It has been demonstrated that under periodic reduction and oxidation, high-index planes of Pt (*e.g.*, Pt(210)) are more stable than low-index planes (*e.g.*, Pt(111)).[14,45–48] This indicates that the square-wave potential plays a key role in the formation of THH Pt NCs. As illustrated in Fig. 6, oxides or hydroxides (O_{ad}, OH_{ad}), originating from the dissociation of H_2O in solution, can readily form on the surface of Pt nanocrystals at +1.20 V *vs.* SCE. Low-index facets of {111} and {100} are smooth with highly coordinated atoms (CNs are 9 and 8, respectively), so oxygen atoms preferentially diffuse/invade into the lattice and replace Pt atoms.[48,49] After desorption of oxygen atoms from the lattice at lower potential (*e.g.* −0.20 V), those displaced Pt atoms cannot always return to their original positions, so that the ordered surface structure will be destroyed, and the close packed structure will be opened. In contrast, since high-index facets contain many step/kink atoms with low CNs (*e.g.*, 6 on Pt(730)), the oxygen atoms preferentially adsorb at such sites without replacing them, and the surface order is preserved. Further theoretical studies are still needed to reveal the detailed microscopic processes of oxygen adsorption on different Pt single crystalline surfaces.[50,51]

Although ascorbic acid was found not to be the key factor for the formation of high-index facets (as mentioned above), other additives in solution were found to affect the final surface structures of Pt nanocrystals during their formation. For example, if the ascorbic acid was replaced by sodium citrate during square-wave potential treatment, concave hexoctahedral Pt nanocrystals were obtained.[52] This new nanocrystals is enclosed by 48 {*hkl*} facets with kink atoms. In Fig. 7a, we can observe that on such Pt nanocrystals, six facets intersect on the point A to give a threefold symmetry, and four facets intersect on the point B to give fourfold symmetry. This symmetry is identical to that of the convex hexoctahedral model shown in Fig. 2. The {*hk*0} facets consist of {100} and {110} microfacets (Fig. 4d), while {*hkl*} facets have additional microfacets of {111}. The formation of concave hexoctahedral Pt nanocrystals in the solution containing sodium citrate indicates that citrate ions promote the formation of {111} microfacets. Previous studies by Xia and co-workers have shown that citrate ions similarly promote the formation of {111} facets on Pd nanocrystals.[53]

In addition to well-defined single crystalline nanocrystals, multi-twinned Pt nanocrystals with high-index facets can also be prepared through the control of the nucleation conditions. For example, if a GC electrode loaded with Pt nanospheres was exposed in air for 3–5 h, new Pt nanocrystals could barely grow on the GC surface during the treatment of square-wave potential, and Pt nanorods grew on the Pt nanospheres instead.[52] As shown in Fig. 7b, the as-prepared Pt nanorod is not uniform in diameter along the longitudinal axis; being broadest at the middle and gradually tapering at both ends. Selected-area electron diffraction (SAED) studies indicate that the Pt nanorod is of fivefold twinned structure. Unlike typical fivefold twinned Au, Ag and Cu nanorods with {111} facets at the end and {100} facets on the side,[54–57] the Pt nanorod is bounded by {*hk*0} facets. The sharp end is enclosed by {410} facets, and the middle part mainly by zigzag-arranged {520} facets, and the obtuse end rooted at the Pt nanospheres is enclosed by {320}, {210} or {730} facets.[52] Clearly, on the surfaces from the obtuse end to the sharp end, the density of step atoms decreases, while crystal growth rate increases. This fact suggests that the density of step atoms on Pt surfaces is a compromise between the crystal growth and oxygen-induced surface reconstruction. This may provide an approach to finely tune the surface structure of Pt surfaces.

One shortcoming of the above high-index faceted Pt nanocrystals is that they all have relatively large size (> 20 nm) and deposited on glassy carbon, which obstruct their potential applications such as in fuel cells due to low Pt utilization efficiency.[58,59] In addition, practical Pt electrocatalysts are usually supported on carbon black. Through changing the precursors, *e.g.*, the employment of insoluble Cs_2PtCl_6

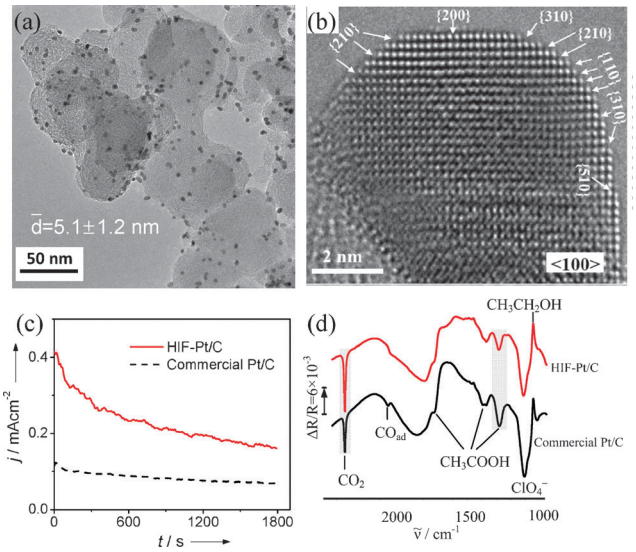

Fig. 8 (a) TEM and (b) aberration-corrected HRTEM images of HIF–Pt/C catalysts. Electrocatalytic properties of HIF–Pt/C and commercial Pt/C for ethanol oxidation. (c) Current–time curves measured at 0.25 V in 0.1 M CH_3CH_2OH + 0.1 M $HClO_4$; (d) Electrochemical *in situ* FTIR spectra at 0.60 V to identify oxidation products (modified with permission from ref. 60, copyright 2010, Wiley-VCH).

nanoparticles dispersed on carbon black instead of large Pt nanospheres, Zhou *et al.*[60] have synthesized high-index faceted Pt nanocrystals supported on carbon black (HIF–Pt/C) with a size (2–10 nm) comparable to that of commercial Pt catalysts (Fig. 8). Aberration-corrected HRTEM (Fig. 8b) and cyclic voltammetric characterizations confirmed that the HIF–Pt/C catalyst contains a much higher density of step atoms than that of commercial Pt/C catalyst. The HIF–Pt/C exhibits a catalytic activity 2–3 times higher than commercial Pt/C catalyst (Johnson Matthey, Inc.) for ethanol electrooxidation (Fig. 8c). Besides, the reaction selectivity is also significantly different. Ethanol can be oxidized to acetic acid or CO_2 with the latter process being more desirable, since its energy conversion efficiency is nearly three times higher than the former, when ethanol is fed into fuel cells. Electrochemical *in situ* FTIR spectra reveal that the low-coordinated step atoms on the HIF–Pt/C catalyst can promote the cleavage of the strong C–C bond of ethanol to generate CO_2, and that the HIF–Pt/C catalyst can produce more CO_2, and less acetic acid than the commercial Pt/C catalyst (Fig. 8d). Quantitative analysis indicates that the selectivity to CO_2 on the HIF–Pt/C catalyst is double that of the Pt/C catalyst.

It should be pointed out that although Pt nanocrystals of small size in the HIF–Pt/C have a high density of step atoms, most of their shapes are not well defined, in comparison to large Pt nanocrystals as stated above. One question arises: what is the smallest size of THH Pt NCs that may be prepared? Molecular dynamics (MD) simulations demonstrate that the thermal stability of THH Pt NCs of 4 nm is similar to that of other shaped Pt nanocrystals (*e.g.*, cube, sphere, cuboctahedron).[43,61] Therefore, it is possible to prepare perfect THH Pt NCs with a size within 10 nm.

It is exciting that a great progress has been also made in the synthesis of Pt NCs with high-index facets by wet chemistry methods. Very recently, Xia and co-workers have reported the synthesis of Pt concave nanocubes mainly enclosed by {720} facets (Fig. 9A).[62] The Pt concave nanocubes exhibit 2–4 times enhanced specific activity for oxygen reduction reaction (ORR) relative to those of Pt nanocubes, cuboctahedra and commercial Pt/C catalysts, that are mainly bounded by

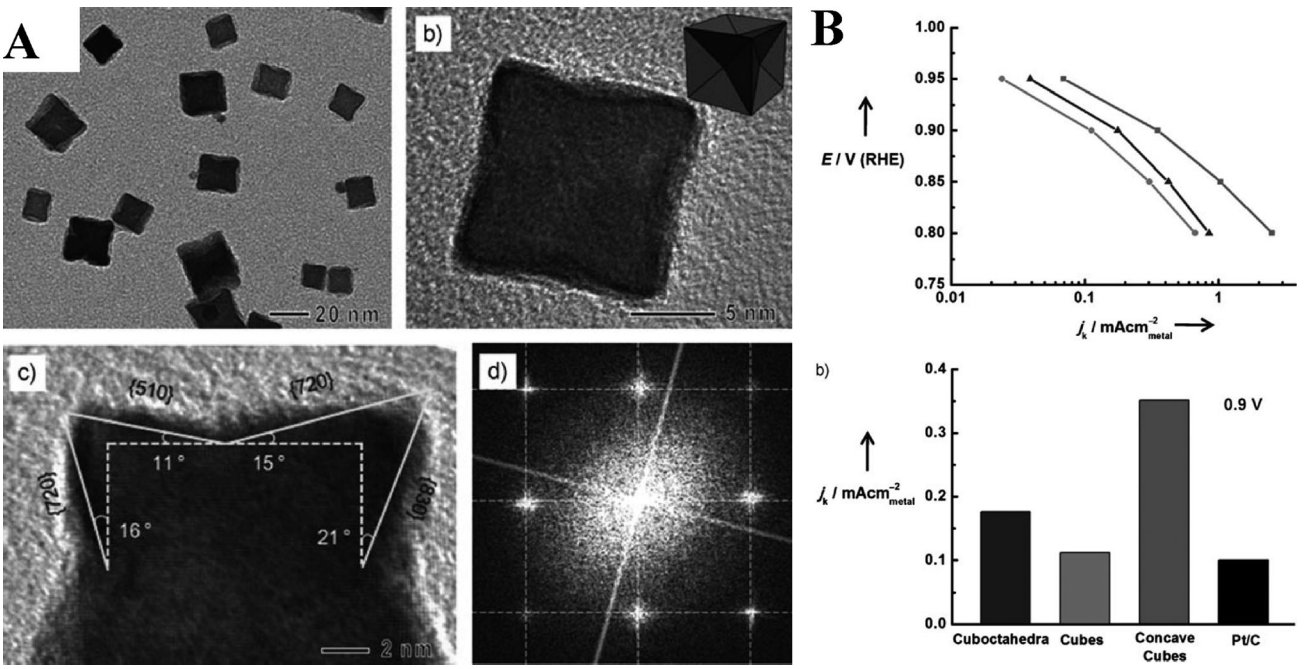

Fig. 9 (A) Low- and high-magnification TEM images of Pt concave nanocubes, FT pattern of a concave nanocube recorded along the [001] zone axis. (B) Comparison of the electrocatalytic activity for oxygen reduction on Pt concave cubes (■), cubes (●) and cuboctahedra (▲) (modified with permission from ref. 62, copyright 2011, Wiley-VCH).

low-index facets such as {100} and {111} (Fig. 9B). A similar method can also be extended to the synthesis of Rh concave nanocubes with a large fraction of {110} facets.[63] The synthesis of Pt concave nanocubes consists of slow reduction of Pt pyrophosphate complex (formed by mixing K_2PtCl_4 and $Na_2H_2P_2O_7$) by $NaBH_4$ in presence of KBr at 95 °C in air. The formation of Pt concave nanocubes was attributed to two indispensable conditions: (1) slow reduction rate and (2) selective chemisorption of Br^- on {100} facets. The slow reduction rate, achieved by the employment of very stable Pt precursors (pyrophosphate complex) and slow addition of the precursors, will facilitate Pt atoms tending to the edges and corners of a seed rather than the entire surface, thus leading to the formation of a concave structure. The selective chemisorption of Br^- ions on the {100} facets of Pt nanocrystals reduces the growth rate along the ⟨100⟩ axis, thus facilitating the formation of nanocubes. One shortcoming of this study is that the real surface structures of Pt concave nanocubes are not very clear yet. The adsorption/desorption of hydrogen and oxygen on the Pt concave nanocubes did not show well-defined voltammetric features. Besides, it is very difficult to provide direct evidence of surface atom arrangement by HRTEM examination due to the concave shape. In addition to polyhedral shapes, Li *et al.* synthesized multipod-like Pt nanostructures with a considerable fraction of {110} facets by using specific peptides (Ac-Thr-Leu-His-Val-Ser-Ser-Tyr-$CONH_2$) as capping agent, which can preferably bind onto {110} facets.[64]

3.2 Pd

Pd nanostructures are of great interest due to their extensive applications in gas sensors and diverse catalytic fields, such as electrooxidation of formic acid and ethanol, automotive exhaust purification, and Suzuki or Heck coupling reactions.[65–69] Recently, considerable progress has been made in shape-controlled synthesis of Pd NCs with high surface energy and open surface structure including high-index and {110} facets.

Since Pd exhibits electrochemical properties (such as potential-induced oxygen adsorption/desorption) similar to that of Pt, but less stable and with a hydrogen absorption feature, the electrochemical square-wave potential method may be also used, with some modifications, for the preparation of Pd nanocrystals with high-index facets. Two high-index faceted Pd nanocrystals, trapezohedral Pd NCs with {*hkk*} facets and concave hexoctahedral Pd NCs with {*hkl*} facets have already been synthesized.[52] Fig. 10a shows a SEM image of a trapezohedral Pd NC, on which four facets surrounded by eight additional facets can be seen. This feature is consistent with the model of a trapezohedron bounded by 24 {*hkk*} facets (Fig. 2). By comparison of SEM image of trapezohedral Pd NCs with the trapezohedral models (Fig. 10b) of various Miller indices, the trapezohedral Pd NC was determined to be most likely bounded by {311} facets. Fig. 10d displays the SEM image of a concave hexoctahedral Pd NCs, whose shape is similar to the model of a concave hexoctahedron bounded by {321} facets (Fig. 9e).

To prepare THH Pd NCs, Tian *et al.* developed a modified method.[70] As illustrated in Fig. 11, THH Pd NCs were directly

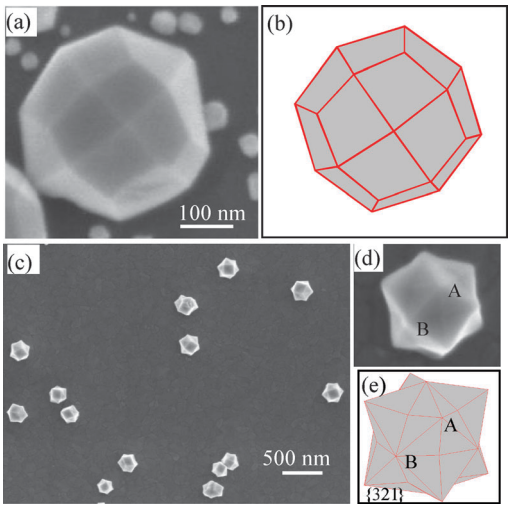

Fig. 10 SEM images of (a) trapezohedral Pd NCs with {*hkk*} facets and (c, d) concave hexoctahedral Pd NCs with {*hkl*} facets synthesized by the electrochemical square-wave potential method. The models of (b) trapezohedron with {311} facets and (e) concave hexoctahedron with {321} facets are also shown (modified with permission from ref. 52, copyright 2008, Royal Society of Chemistry).

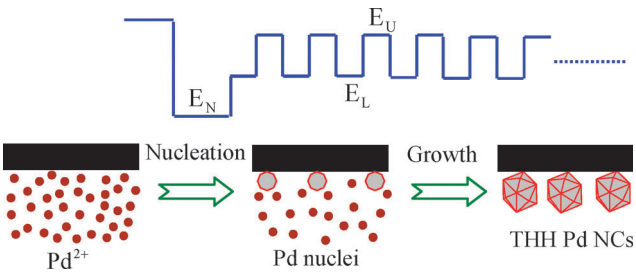

Fig. 11 Illustration of programmed electrodeposition method for preparation of THH Pd NCs (modified with permission from ref. 70, copyright 2010, American Chemical Society).

electrodeposited (from solution) on the GC substrate in 0.2 mM $PdCl_2$ + 0.1 M $HClO_4$ solution by a programmed electrodeposition method. In this method, the GC electrode was first subjected to a potential step from 1.20 to −0.10 V (E_N) for 20 ms to generate Pd nuclei. The growth of the Pd nuclei to THH Pd NCs was achieved by applying a square-wave potential (f = 100 Hz) with E_L and E_U of 0.30 and 0.70 V, respectively. Note that the E_U for preparation of Pd is much lower than that for Pt (E_U = 1.20 V), since Pd can be oxidized more easily. Obviously, the synthesis method for THH Pd NCs is simpler than that for THH Pt NCs.[30] The difference between the two synthesis routes lies in the source of Pt or Pd ions. During the preparation of THH Pt NCs (a two-step method), Pt nanospheres partly dissolve and provide the ions for growth of THH Pt NCs. After the growth process has been terminated, some residual polycrystalline nanospheres may be left over on the GC substrate. This creates a bimodal mixture of particles and non-uniform surface. The simpler one-step synthesis of Pd nanocrystals produces a mono-modal particle size distribution and leads to no waste of precious metal.

The SEM image of as-prepared THH Pd NCs is shown in Fig. 12a. The yield of the THH Pd NCs is over 80%, and the

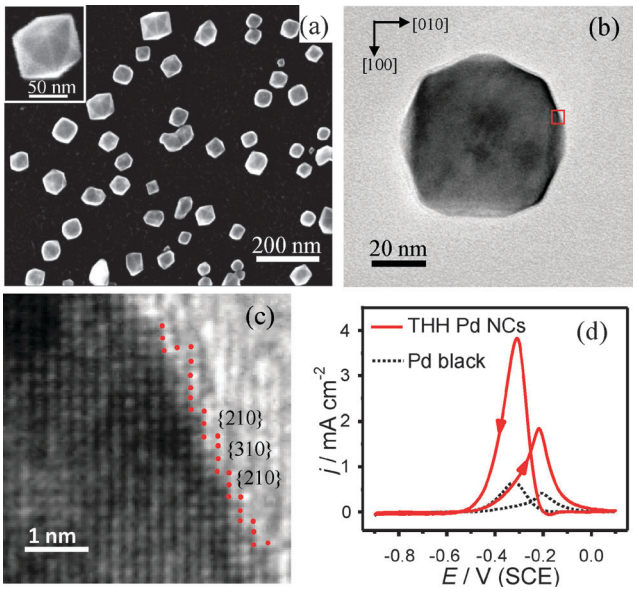

Fig. 12 (a) SEM image of THH Pd NCs. The inset is a high-magnification SEM image. (b) TEM image of a THH Pd NC recorded along the [001] direction. (c) HRTEM image recorded from the boxed area in (b), showing some {210} and {310} steps that have been marked by red dots. (d) Cyclic voltammograms of THH Pd NCs (solid line) and Pd black catalyst (dashed line) at 10 mV s^{-1} in 0.1 M ethanol + 0.1 M NaOH (modified with permission from ref. 70, copyright 2010, American Chemical Society).

other shapes are agglomerations of imperfect THHs and irregular polyhedra. The average size of THH Pd NCs was 61 nm. The exposed facets on the THH Pd NCs are also mainly {730} facets, as determined by HRTEM and SAED. The {210} and {310} steps can be discerned on the border atoms in the HRTEM image, as marked in Fig. 12c. Owing to their high density of surface active sites, the THH Pd NCs exhibited 4–6 times higher catalytic activity per unit surface area when compared to commercial Pd black catalyst (Johnson Matthey, Inc.) for ethanol electrooxidation in alkaline solutions (Fig. 12d). Besides, the THH Pd NCs also exhibits a high stability. After 1000 potential cycles, 75.0–95.5% of the initial catalytic activity could be still maintained.

It is worthwhile noting that the $PdCl_2$ concentration is a vital factor for the growth of THH Pd NCs. If the [$PdCl_2$] is increased from 0.2 to 1.0 mM, twinned Pd nanorods appear. Especially, when the [$PdCl_2$] is increased to 5.0 mM, the nucleation step becomes unnecessary and fivefold-twinned Pd nanorods with {*hkk*} or {*hk*0} high-index facets are produced.[71] The Pd nanorods with {*hkk*} facets were synthesized at $E_L = -0.15$ and $E_U = 0.65$ V. As shown in Fig. 13a and b, the tip of the Pd nanorods is an elongated pentagonal pyramid. By measurement of the geometric parameters (*e.g.*, the ratio of height to base width) of the nanorod tip, the surfaces of the Pd nanorods was determined to be ranging from {10,1,1} to {15,1,1} facets. With increasing square-wave potential ($E_L = 0.15$ V and $E_U = 0.85$ V), another type of Pd nanorods with {*hk*0} facets was synthesized, as shown in Fig. 13d and e, the tip of the synthesized Pd nanorods has changed into a decagonal pyramid and the surfaces vary from {310} to {610} facets. The difference in surface structure on the two types of Pd nanorods indicates that more intensive surface reconstruction by oxygen adsorption/desorption (E_U: 0.85 *vs.* 0.65 V) will favor the formation of surfaces with lower coordinated atoms (CNs are 6 and 7 for {*hk*0} and {*hkk*}, respectively). For ethanol electrooxidation in alkaline solutions, the catalytic activity of Pd nanorods with {*hkk*} facets is 2–3 times that of commercial Pd black catalyst from Johnson Matthey, Inc. (Fig. 13c), and the enhanced factor is even higher on Pd nanorods with {*hk*0} facets (3–5 times that of Pd black, Fig. 13f).

Besides the electrochemical square-wave potential method outlined above, Pd NCs with {110} and {730} facets have also been synthesized successfully by using wet chemistry methods or conventional electro-deposition.[72–75] Xia and co-workers first reported the chemical synthesis of Pd nanorods with {110} facets.[72] The synthesized Pd nanorods are of single crystalline structure, and bounded by four {100} facets and four {110} facets arranged alternately on the side faces (Fig. 14a and b). The chemisorption of bromide on the Pd seed was considered to promote the formation of {100} and {110} facets. By using a conventional electrodeposition method, Zhuang and co-workers[74] also prepared Pd nanorods with exposed {110} facets (Fig. 14c). They found that Pd nanorods exhibit very high electrocatalytic activity for oxygen reduction. At 0.85 V, a practical operating potential of a PEMFC cathode, the kinetic current density of Pd nanorods approaches that of Pt, and is 10-fold higher than that of Pd nanoparticles (Fig. 14d). They rationalized the high catalytic activity to exceptionally weak adsorption of oxygen on Pd(110) through DFT calculations. In addition to Pd nanorods, some highly branched Pd nanostructures with high density of step atoms (such as {311} microfacets) near Pd tips are also prepared, and exhibit high electrocatalytic activity towards formic acid oxidation.[76–79]

Recently, polyhedral Pd NCs of open surface structure have also been successfully synthesized by wet chemistry methods. Zheng *et al.*[73] have synthesized concave tetrahedral and concave trigonal-bipyramidal Pd nanocrystals bound with {111} and {110} by a solvothermal method (Fig. 15). The concave tetrahedron can be considered as a tetrahedron with each face excavated by a trigonal pyramid. The concave surfaces of the trigonal pyramid were assigned to {110} facets. The synthesis was carried out in a Teflon lined stainless-steel autoclave containing $Pd(acac)_2$, PVP and formaldehyde dissolved in benzyl alcohol. They considered that the formaldehyde plays a key role for the formation of concave Pd nanocrystals, since the degree of concavity of the Pd nanocrystals is increased with increasing concentration of formaldehyde (Fig. 15a–c). Correspondingly, the electrocatalytic activity of Pd nanocrystals for formic acid oxidation is also increased (Fig. 15d).

Xu and co-workers[75] reported the synthesis of rhombic dodecahedral Pd nanocrystals enclosed by 12 {110} facets by a seed-mediated method. The method involves the use of Pd nanocubes (22 nm) as seeds, cetyltrimethylammonium bromide (CTAB) as surfactant, KI as additive and ascorbic acid as reductant. The developed method is very versatile. Rhombic dodecahedral, cubic and octahedral Pd nanocrystals, as well as their transition shapes could be selectively synthesized by

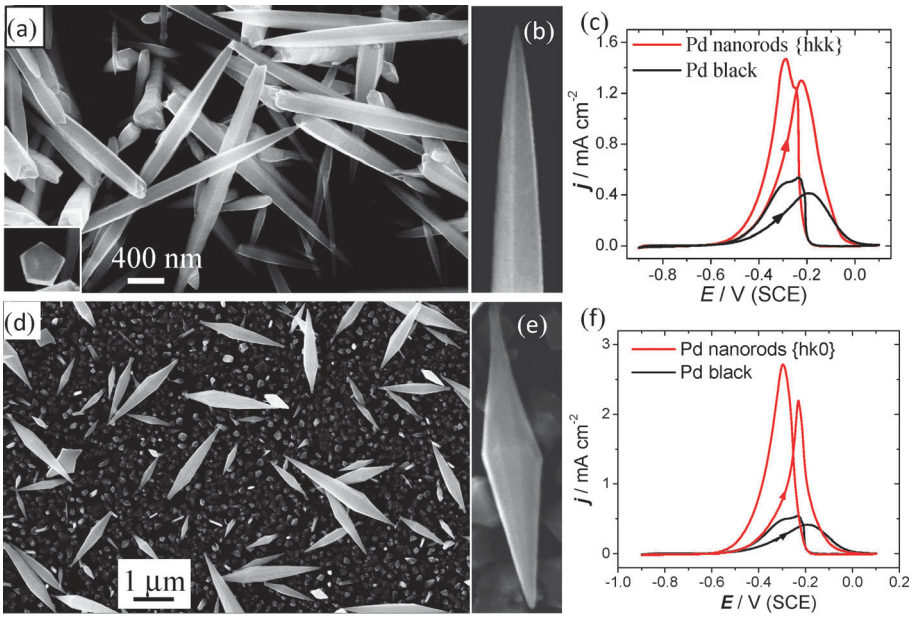

Fig. 13 SEM images of Pd nanorods with {*hkk*} facets (a, b) and with {*hk*0} facets (d, e); Electrocatalytic comparison between Pd nanorods and commercial Pd black catalyst for ethanol electrooxidation (c, f). 10 mV s^{-1}; 0.1 M ethanol + 0.1 M NaOH (modified with permission from ref. 71, copyright 2009, Royal Society of Chemistry).

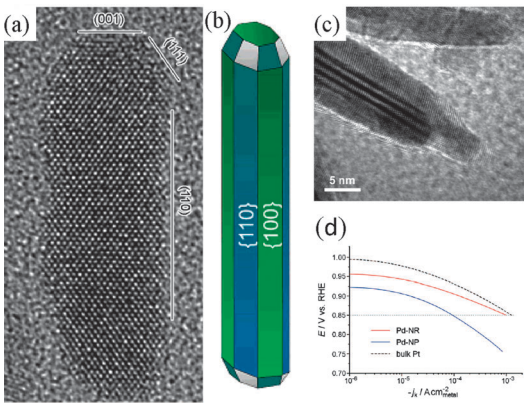

Fig. 14 (a) High-resolution TEM images of a Pd nanorod recorded along [1$\bar{1}$0]. (b) The model of Pd nanorod (modified with permission from ref. 72, copyright 2007, American Chemical Society). (c) TEM image of Pd nanorods electrodeposited on carbon powder. (d) Comparison of electrocatalytic activity for oxygen reduction between Pd nanorods (red line), Pd nanoparticles (blue line) and bulk Pt electrode (dashed line) in O_2-saturated 0.1 M $HClO_4$ (modified with permission from ref. 74, copyright 2009, American Chemical Society).

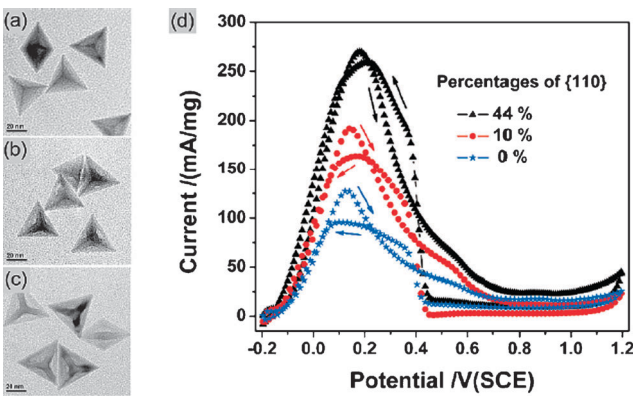

Fig. 15 (a–c) TEM images and (d) electrocatalytic properties of concave tetrahedral Pd nanocrystals with different percentages of {110} facets. The CV curves were recorded in 0.5 M H_2SO_4 + 0.25 M HCOOH solution at a scan rate of 50 mV s^{-1} (modified with permission from ref. 73, copyright 2009, American Chemical Society).

simply varying the concentration of KI and reaction temperature (Fig. 16). The {110} facets of Pd are favored at relatively high temperatures and medium KI concentrations.

Although wet chemical synthesis of pure Pd polyhedral nanocrystals with high-index facets have not been reported, Pd nanoshells with high-index facets have been realized very recently though overgrowth on Au nanocrystals.[80–82] Lu *et al.* first synthesized Au_{core}–Pd_{shell} heterostructures with THH morphology by using Au nanocubes as the structure-directing cores.[80] The THH nanocrystals are bounded by high-index {730} facets (Fig. 17a). They identified four key factors facilitating the formation of the THH core–shell nanocrystals, as illustrated in Fig. 17b. They are: (1) a substantial lattice mismatch between Au and Pd; (2) oxidative etching in the presence of chloride and oxygen; (3) the use of cetyltrimethylammonium chloride (CTAC) surfactant; (4) moderate reaction temperature (30–60 °C).[80] In comparison with the electrochemical square-wave potential method (Fig. 6 and Fig. 17b), the respective oxidation–reduction reactions for growth of high-index facets are similar. Yu *et al.* prepared polyhedral Au@Pd NCs with three different classes of high-index facets, including concave trisoctahedral NCs with {*hhl*} facets, concave hexoctahedral NCs with {*hkl*} facets and THH NCs with {*hk*0} facets.[81] The key for the preparation is heteroepitaxial growth of Pd layers on concave trisoctahedral gold NC seeds under carefully controlled Pd/Au ratio and NaBr concentration. The Miller indices of NCs are also

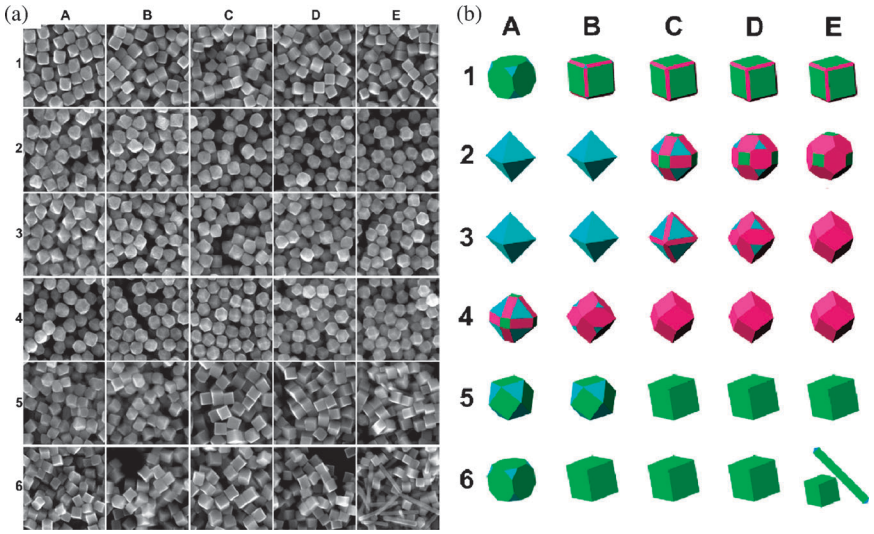

Fig. 16 (a) SEM images of polyhedral Pd nanocrystals synthesized under different conditions. (b) Corresponding geometrical models of Pd nanocrystals. The {100}, {111} and {110} facets are shown in green, blue and purple, respectively (modified with permission from ref. 75, copyright 2010, American Chemical Society).

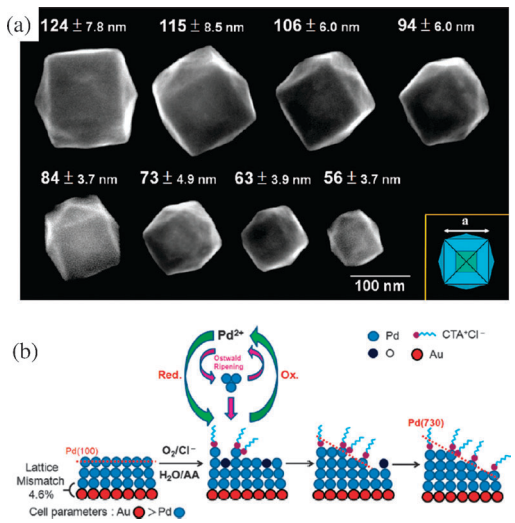

Fig. 17 (a) Representative SEM images of the THH Au_{core}–Pd_{shell} nanocrystals synthesized with sizes varying from 56 to 124 nm. (b) Schematic illustration of the formation of {730} facets (modified with permission from ref. 80, copyright 2010, American Chemical Society).

modifiable, *e.g.*, from {210} to {720} for THH NCs. They found that Au@Pd NCs with high-index facets were more active for formic acid oxidation at low potentials than those with low-index facets with an order of cubes < octahedra < concave trisoctahedra < concave hexoctahedra < $THH_{\{720\}}$ < $THH_{\{210\}}$ < $THH_{\{520\}}$.[81] By a similar approach, Wang *et al*. have also prepared Pd nanoshells with high-index {730} and {221} facets through heteroepitaxial growth on corresponding high-index-faceted Au nanocrystals (*i.e.*, tetrahexahedron and trisoctahedron). The catalytic activity of the high-index-faceted Pd nanoshells for the Suzuki coupling reaction is 3–7 times those of Pd and Au–Pd core-shell nanocubes, which possess only {100} facets. It is worth pointing out that the surfaces of Pd nanoshells prepared by Wang *et al.*[82] are much smoother (especially for THH) than the other two cases above.[80,81]

As for the growth mechanism, Xia and co-workers proposed that oxidative etching of crystal nuclei or seeds by O_2 with the assistance of Cl^-, Br^- and Fe^{3+} coexisting in the reaction solution often occurs, since most syntheses are conducted in air.[34] In this case, the oxidative etching and chemical reduction occur simultaneously during the synthesis processes. They may also be considered as periodic oxidation–reduction reactions, as that induced by electrochemical square-wave potential method. If the relative rate of chemical reduction and oxidative etching can be finely tuned, then wet chemistry methods for synthesizing nanocrystals of high surface energy and open surface structure may be further developed.

3.3 Au

Au nanomaterials have wide use in surface plasmon resonance (SPR), surface-enhanced Raman scattering (SERS) and biomedicine. Gold nanomaterials have also attracted intense interest in recent years following the discovery that small (*ca.* 3 nm) supported Au nanoparticles could be effective catalysts for CO oxidation at low temperatures.[83] The shape-controlled synthesis of Au nanocrystals with well-defined shapes has been carried out for over ten years. Unlike Pt and Pd, the synthesis of Au nanocrystals with high surface energy and open surface structure by conventional wet chemistry methods is relatively easy, and great progress has been made. The main reason may be attributed to the relatively small difference in surface energy between low-index and high-index planes of Au, in comparison with Pt-group metals.[9] One shortcoming is that since the size of the obtained Au nanocrystals with open surface structure is usually very large (> 10 nm), the studies of catalytic properties are difficult to perform. Herein, we mainly illustrate their synthesis.

In 1997, Yu *et al*. synthesized Au nanorods by using an electrochemical method (Fig. 18a),[84] and surface structures of

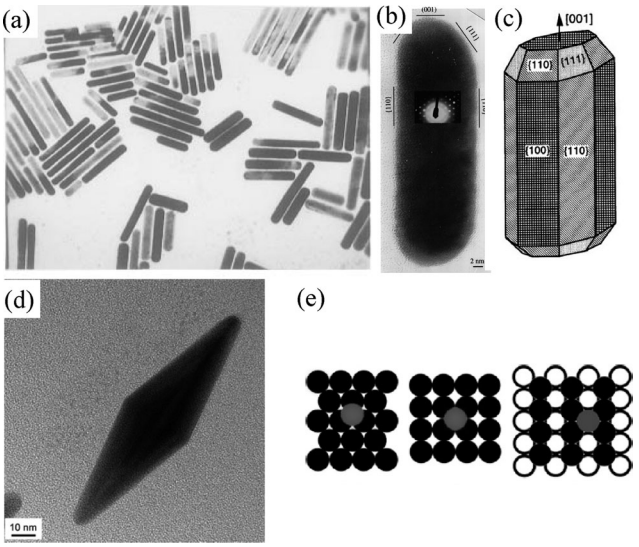

Fig. 18 (a) Low-magnification TEM image of Au nanorods prepared by an electrochemical method (modified with permission from ref. 84, copyright 1997, American Chemical Society). (b) High-magnification TEM image of Au nanorod and (c) structure model of the Au nanorod with {110} facets (modified with permission from ref. 85, copyright 1999, Elsevier). (d) TEM image of an Au nanobipyramid and (e) schematic illustration of UPD Ag (gray circle) on Au(111), Au(100) and Au(110) surfaces. Each Ag atom has 3, 4 and 5 nearest neighbors on these three surfaces (modified with permission from ref. 86, copyright 2005, American Chemical Society).

the Au nanorods were identified thereafter by Wang *et al.* through HRTEM studies in 1999.[85] As shown in Fig. 18b and c, the nanorods are single crystals, grown along the [100] direction with side walls as the {110} and {100} facets. By using an Ag(I)-assisted seed-mediated method, Liu *et al.* synthesized two types of Au nanocrystals with open surface structure. One is the above-mentioned single crystalline Au nanorods with {110} and {100} facets, and the other is Au elongated bipyramids of fivefold twinned structure (Fig. 18d).[86] Similar to the Pd nanorods shown in Fig. 13a, the elongated Au bipyramids are also bounded by high-index facets of {*hkk*}. By measuring the tip angle, they determined that the surfaces were indexed as (711). More importantly, Liu *et al.* provided a reasonable growth mechanism for the formation of Au nanorods with open surface structure.[86] In the reaction solution, the weak reductant ascorbic acid leads to the formation of a silver monolayer on Au surfaces (*i.e.* chemical-induced underpotential deposition). As shown in Fig. 18e, on the {110} or {711} facets with open surface structure, the Ag atom has more nearest neighbors (*e.g.*, 3 on {111}, 4 on {100} and 5 on {110} or {711} facets). Therefore, the Ag monolayer is preferably formed on the {110} or {711} facets. These monolayer atoms of Ag act as a strongly binding surfactant to protect the facet from further growth. Although the silver monolayer can be oxidized and replaced by the gold ions in the solution, the total growth rate of gold on {110} or {711} facets may be significantly slowed down. As a consequence, the {110} or {711} facets can be preserved in the final products. In addition to the rod shape, single crystalline Au nanobelts with {110} facets were synthesized by Chen *et al.*[87] through directional solidification of the Fe–Au eutectoid followed by selective phase dissolution. The Au nanobelts have an extremely high aspect ratio of more than 1500 (thickness of 25–30 nm, width of 200–250 nm and length of 20 μm). After cleaning the surfaces by PbO_2 deposition/dissolution, the Au nanobelts possess (110) domains over 65%, and exhibit considerably higher catalytic activity than polycrystalline Au electrode towards methanol electrooxidation in alkaline solutions.[88]

Liao *et al.*[89] have synthesized another type of fivefold twinned Au nanocrystals with high-index facets, *i.e.* star-shaped Au nanocrystals in deep eutectic solvents (DES)—a solvent with properties similar to ionic liquids. As shown in Fig. 19, each branch of the star-shaped Au nanocrystals is a tetragonal pyramid that protrudes along the [001] direction. The four side faces of each tetragonal pyramid are (331) and vicinal high-index facets, all having a high surface energy. Owing to their high-index facets that provide a high density of active sites, the star-shaped Au NCs exhibit high catalytic activity towards H_2O_2 electrocatalytic reduction. In comparison with bulk Au, the enhancement factor is up to 14.

Inspired by the above early work, other researchers have synthesized a large number of polyhedral single-crystal Au NCs with open surface structure. Some typical SEM or TEM images extracted from relevant literature are illustrated in

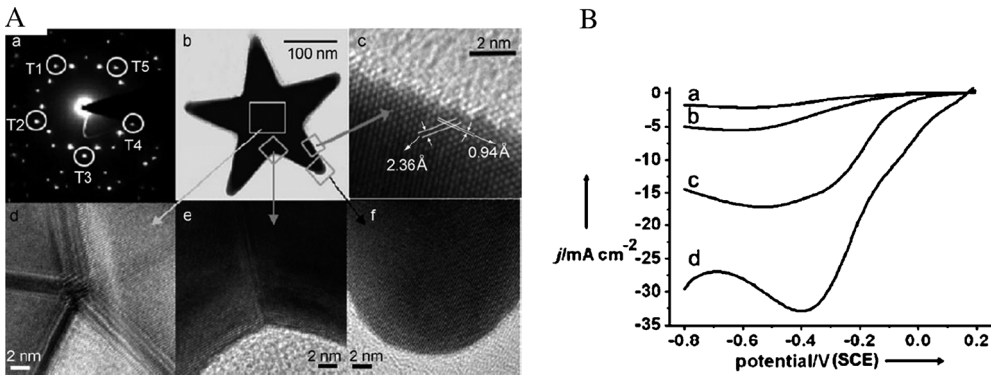

Fig. 19 (A) HRTEM images of star-shape Au nanocrystal recorded along [110] and (B) comparison of electrocatalytic activity for H_2O_2 reduction on different Au surfaces: (a) polycrystalline Au electrode, (b) snowflake-like Au NPs, (c) nanothorns, (d) star-shaped Au NPs (modified with permission from ref. 89, copyright 2008, Wiley-VCH).

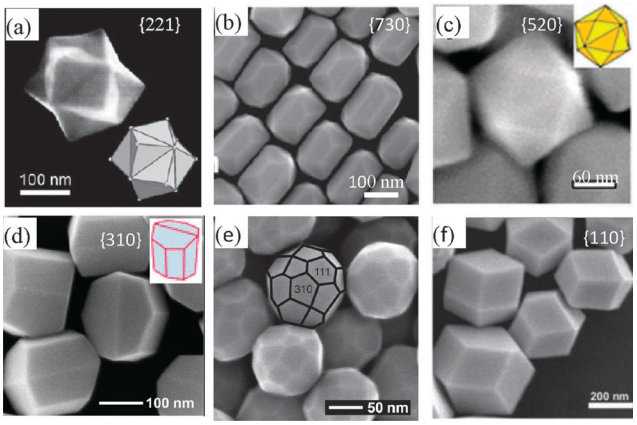

Fig. 20 (a) SEM image of a Au trisoctahedral nanocrystal; inset: model of an ideal trisoctahedron enclosed by {221} surfaces (modified with permission from ref. 90, copyright 2008, Wiley-VCH). (b) SEM image of the elongated THH Au NCs (modified with permission from ref. 92, copyright 2009, American Chemical Society). (c) SEM images of perfect THH Au NCs (modified with permission from ref. 93, copyright 2010, Royal Society of Chemistry). (d, e) SEM images of Au NCs with truncated ditetragonal prism and truncated THH shapes (modified with permission from ref. 96, copyright 2011, American Chemical Society). (f) SEM images of rhombic dodecahedral Au nanocrystals (modified with permission from ref. 99, copyright 2009, American Chemical Society).

Fig. 20. Xie *et al.*[90] first reported the preparation of trisoctahedra Au NCs enclosed by 24 high-index {221} facets by reduction of an aqueous solution of $HAuCl_4$ with ascorbic acid in the presence of CTAC (Fig. 20a). Thereafter, Yu *et al.* successfully synthesized concave trisoctahedral Au NCs bounded by high-index {*hhl*} facets by a seed-mediated growth method also using CTAC as the capping agent.[91] They considered that the formation of these trisoctahedral NCs was kinetically driven and governed by two main factors: (i) the preferential face-blocking adsorption of CTA^+ on high-index facets and (ii) a favorable reduction rate of the metal ions in the growth solution.

THH Au NCs were first synthesized by Ming *et al.*[92] through a seed-mediated growth in a mixture containing ascorbic acid, $HAuCl_4$, Au seeds, CTAB and $AgNO_3$. The obtained THH Au NCs show elongated shapes (Fig. 20b) and their surfaces are identified as {730} facets. Thereafter, Li *et al.*[93] prepared more perfect THH Au NCs with exposed {520} facets (Fig. 20c), also by using the seed-mediated growth with mixed surfactants (didodecyldimethylammonium bromide (DDAB) and CTAB). Their THH Au NCs possess enhanced electrocatalytic activity toward the oxidation of formic acid. Zhang and co-workers[94] found that if the CATB was replaced by CTAC, concave THH Au NCs with {720} facets could be produced. In the above three cases, $AgNO_3$ is used during seed-mediated growth. As a result, the formation of high-index facts is also likely *via* the mechanism proposed by Liu *et al.*[86] Besides the seed-mediated methods, Kim *et al.*[95] synthesized THH Au NCs with {210} facets and rhombic dodecahedral Au NCs with {110} facets by simply reducing $HAuCl_4$ in a mixed solution of *N*,*N*-dimethylformamide (DMF) and poly(vinylpyrrolidone) (PVP). However, the surfaces of the Au NCs obtained are not smooth like those reported by Ming *et al.*[92] and Li *et al.*[93] It is interesting that high-index faceted Au polyhedral nanocrystals with lower symmetry, such as ditetragonal prism shape with truncated ends (polyhedron with 12 facets, Fig. 20d), truncated tetrahexahedra (Fig. 20e), have also been reported.[96,97]

Rhombic dodecahedral Au NCs enclosed by 12 {110} facets can be synthesized by a variety of methods and the shape evolution from rhombic dodecahedron to octahedron or cube can be achieved through suitable changes of reaction conditions.[98–102] Fig. 20d illustrates perfect rhombic dodecahedral Au NCs synthesized by Jeong *et al.* who only used *N*,*N*-dimethylformamide (DMF) as both reductant and solvent.[99] In addition to rhombic dodecahedra, Wang *et al.* reported a new shape of Au nanocrystals, *i.e.* singly twinned squashed dodecahedron also bounded by {110} facets.[103]

3.4 Fe

Fe is the fourth most abundant element on earth. The most important application of Fe nanoparticles is used as catalysts in ammonia synthesis. In addition, Fe materials also play a very important role in denitrification of agricultural fertilizers which would otherwise cause severe nitrate/nitrite pollution of water sources. The most stable lattice of Fe is the body-centered cubic (bcc) structure. Unlike fcc lattice metals, Fe(111) has the most open surface structure and thus the highest surface energy among Fe crystal planes, while Fe(110) is the closest-packed surface. Somorjai and co-workers[104] have demonstrated that surface structures of Fe catalysts have a significant impact on their catalytic activity for ammonia synthesis, and found that the activity ratio of (111) : (100) : (110) single-crystal planes was as high as 418 : 25 : 1. Unlike Pt, Pd and Au, there are very few reports about shape-controlled synthesis of Fe nanocrystals.

Chen *et al.* first reported the shape-controlled synthesis of Fe nanocrystals by an electrochemical route.[105,106] Through careful control of the nucleation and growth by varying the electrochemical conditions (*e.g.*, the deposition potential and the concentration of $FeSO_4$ in solution), they obtained two series of Fe nanocrystals enclosed by different crystalline facets (Fig. 21A). One changes from rhombic dodecahedra bounded by {110} facets at a low overpotential to 18-facet polyhedra enclosed by certain combinations of {110} and {100} facets, and finally to cubes exclusively covered by {100} facets at a high overpotential. The other varies from tetragonal bipyramids also bounded by {110} facets to 18-facet polyhedra, and finally to cubes with increasing overpotentials. The evolution of the shapes of Fe nanocrystals with overpotentials may be interpreted by the two-dimensional nuclei theory developed in the 1960s.[107] In this theory, the rate of formation of two-dimensional nuclei is proportional to $\exp(-W_{hkl}/k_BT)$ (where W_{hkl} is the work of formation of the {*hkl*} nuclei, k_B is Boltzman's constant and T is the absolute temperature). The value of W_{hkl} depends on both surface structures and overpotentials. At relatively low overpotentials, low-energy {110} facets have the minimum overall work of formation, so rhombic Fe dodecahedral or tetragonal bipyramidal nanocrystals form. As the overpotential increases, W_{100} becomes

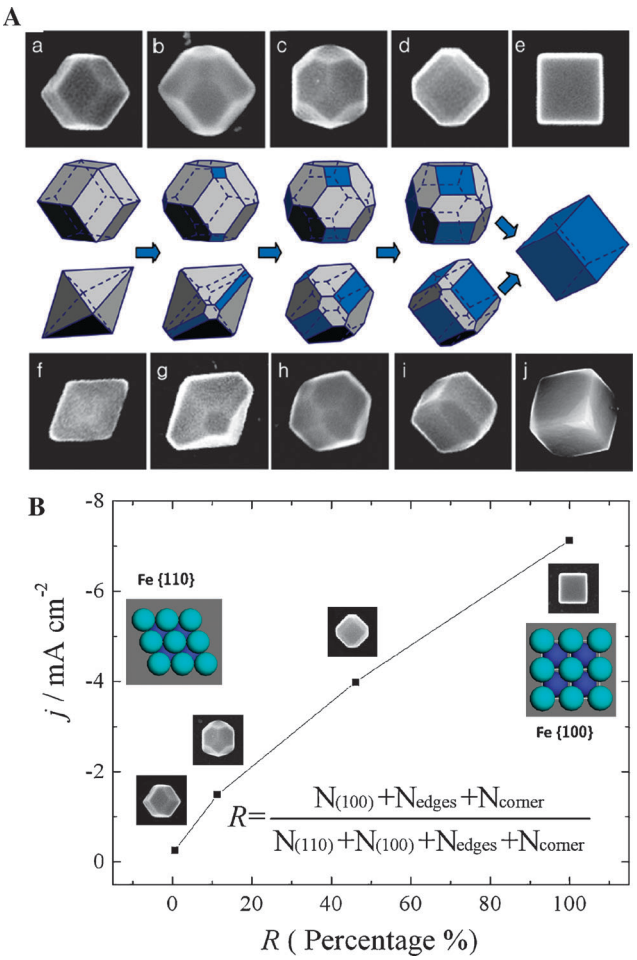

Fig. 21 (A) SEM images of Fe NCs and corresponding models. (a–e) Shape transformation of Fe NCs from rhombic-dodecahedron to a series of 18-facet polyhedral shapes and finally to cubic in 0.002 M $FeSO_4$ + 0.1 M Na_2SO_4. (f)–(j) Shape transformation of Fe NCs from tetragonal bipyramids to a series of 18-facet polyhedral shapes and finally to cubic in 0.02 M $FeSO_4$ + 0.1 M Na_2SO_4. (B) Relationship between electrocatalytic activity of the Fe NCs and the ratio of active surface atoms. (modified with permission from ref. 105, copyright 2009, American Chemical Society).

lower than W_{110}, leading to the formation of the cubic Fe nanocrystals.

The electrocatalytic activity of as-synthesized Fe nanocrystals towards nitrite electroreduction is also surface structure dependent. As shown in Fig. 21B, the catalytic activity increases with increasing fraction of the {100} facets, edge and corner sites. The cubic Fe nanocrystals bounded by {100} facets with relatively high surface energy exhibit the highest activity among the Fe nanocrystals synthesized.

4. Shape-controlled synthesis of metal oxides of high surface energy

Apart from metal nanocrystals, metal oxides with high surface energy have also attracted increasing interest. So far, a series of metal oxides (*e.g.*, TiO_2,[31,108–111] SnO_2,[112] ZnO,[113,114] Cu_2O,[115] α-Fe_2O_3,[116] Fe_3O_4,[117,118] CO_3O_4[114,119] MgO,[114] and composite oxides[15]) and metal sulfides[120] have been synthesized in recent years. Xie *et al.*[32] has reviewed some studies of micro/nanostructured crystallites with high surface energy, mainly focusing on metal oxides. Herein, we just highlight some selected examples including TiO_2, SnO_2 and lithium Mn-rich metal oxides, as well as their potential applications.

4.1 TiO_2

Titanium dioxide (TiO_2) is one of the most important semiconductor materials, and plays an important role in many applications such as photocatalytic decomposition of pollutants, dye-sensitized solar cells, sensors and biomedical materials. TiO_2 has typically three crystal phases: anatase, rutile and brookite, among which anatase exhibits both high stability and high photocatalytic activity. Anatase TiO_2 belongs to tetragonal lattice ($I4_1/amd$), with lattice constants of a = 0.3783 nm and c = 0.951 nm. Theoretical calculation has demonstrated that the order of surface energies of anatase TiO_2 is {110} > {001} > {100} > {101}, and the corresponding values are 1.09, 0.90, 0.53 and 0.44 J m^{-2}, respectively.[121,122] In bulk anatase, Ti atoms are sixfold-coordinated by O atoms, and O atoms are threefold-coordinated by Ti atoms. On (101), the most thermodynamically stable surface, there exist five-fold-coordinated Ti (5c-Ti) and two-coordinated O (2c-O) sites, and the density of the 5c-Ti sites is 5.1 × 10^{14} cm^{-2}.[121] On the {001} surfaces, there are a much higher density of the 5c-Ti sites (7.0 × 10^{14} cm^{-2}); there even exists fourfold-coordinated Ti (4c-Ti) on the {110} surfaces. Due to high density of dangling bonds and high surface energy, the {001} and {110} surfaces are much more reactive than the (101) surface. Unfortunately, most synthetic and natural anatase crystals are dominated by the low surface energy and less-reactive (101) surface. Interestingly, important advances have been made in synthesis of TiO_2 with high surface energy, and some selected cases are reviewed here.

Lu and co-workers made a breakthrough in the synthesis of anatase TiO_2 with high-energy {001} facets.[31] Through systematically investigating the effect of non-metallic atoms X (where X represents H, B, C, N, O, F, Si, P, S, Cl, Br or I) on the surface energies of TiO_2 by first-principle calculations, they found that the termination with F atoms can greatly decrease the surface energy of TiO_2 (Fig. 22a). Furthermore, the F termination can make (001) to be more stable than (101). Based on this theoretical prediction, they used TiF_4 aqueous solution and HF as precursor and crystallographic controlling agent, respectively, to generate truncated anatase bipyramids under hydrothermal conditions. Fig. 22b shows a SEM image of the as-synthesized anatase TiO_2 crystals. The side length of TiO_2 crystals is about 1.6 μm. On the basis of the symmetries of anatase TiO_2, two flat, square surfaces are {001} facets and the eight isosceles trapezoidal surfaces are {101} facets. The percentage of high-energy {001} facets ranges from 35% and 47%.

They further developed a solvothermal method using 2-propanol as a synergistic capping agent and reaction medium together with HF to synthesize high-quality anatase TiO_2 single crystal nanosheets (SCNSs) with {001} facets reaching up to 64% (Fig. 22c).[123] According to the theoretical

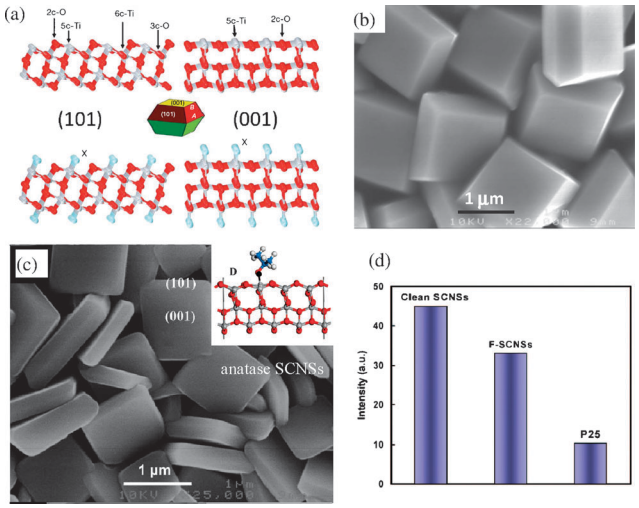

Fig. 22 (a) Slab models of anatase TiO_2 (101) and (001) surfaces. (b) SEM image of anatase TiO_2 single crystals with 35% (001) facets (modified with permission from ref. 31, copyright 2008, Nature Publishing Group). (c) SEM image of anatase TiO_2 single-crystal nanosheets (SCNSs) with 64% (001) facets. (d) Comparison of photocatalytic efficiency for producing •OH radical on clean TiO_2 SCNSs, F-terminated TiO_2 and Degussa P25 TiO_2 (modified with permission from ref. 123, copyright 2009, American Chemical Society).

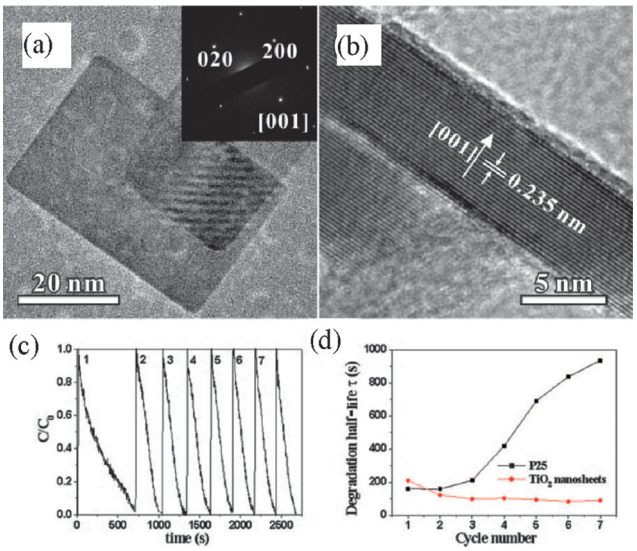

Fig. 23 (a) High-magnification TEM image of an individual TiO_2 nanosheet; the inset shows the corresponding SAED pattern. (b) HRTEM image from the vertical nanosheets. (c) Cycling degradation curve for photocatalytic degradation of methyl orange (MO) on TiO_2 nanosheets [89% (001) facets]. (d) Degradation half-life of MO for TiO_2 nanosheets and commercial P25 TiO_2 (modified with permission from ref. 109, copyright 2009, American Chemical Society).

calculations, they proposed a growth mechanism: under acidic conditions, 2-propanol tends to heterolytically dissociate to form an alkoxy group ($(CH_3)_2CHO$–) bound to coordinatively unsaturated Ti^{4+} cations on the (001) and (101) surfaces. The higher density of the 5c-Ti on (001) surfaces may lead to more obvious selective adhesion of 2-propanol, which retards the growth of anatase TiO_2 single crystals along the [001] direction. The photocatalytic efficiency of anatase TiO_2 SCNSs was monitored by measuring the formation of active hydroxyl radicals (•OH) upon irradiation, which are considered as the most important oxidative species in photocatalysis reactions. As shown in Fig. 22d, the normalized concentration of •OH generated from the F-terminated TiO_2 SCNSs is more than three times higher than that of commercial Degussa P25 TiO_2, a benchmarking material. After the surface F atoms were removed through heat treatment to obtain a clean surface, the photocatalytic activity was further enhanced. The result clearly demonstrates that the high density of unsaturated 5c-Ti on {001} facets can significantly enhance the photocatalytic activity of the anatase TiO_2.

One disadvantage of anatase TiO_2 synthesized by Lu *et al.* is that the crystallite size is relatively large (side length ~1.6 μm), as compared with commercial Degussa P25 TiO_2 (15–25 nm).[124] Xie and co-workers reported a modified hydrothermal route by using tetrabutyl titanate, $Ti(OBu)_4$, as a precursor and 47% HF solution as the solvent, and synthesized sheet-like anatase TiO_2 with the (001) facets ranging from 77 to 89%.[109] As shown in Fig. 23a and b, the as-synthesized TiO_2 consists of well-defined sheet-shaped structures with a rectangular outline, side length of ~40 nm and thickness of ~6 nm. Owing to the high percentage of highly reactive (001) facets, the TiO_2 nanosheets exhibit excellent activity in the photocatalytic degradation of organic contaminants (such as methyl orange), far exceeding that of commercial P25 TiO_2. In addition, some other groups have also reported anatase TiO_2 nanosheets, as well as their spherical assemblies with highly exposed {001} facets.[110,125–130]

Interestingly, Liu *et al.* synthesized anatase TiO_2 single crystals with exposed {001} and {110} facets by using a modified hydrothermal method in the presence of Ti powder, H_2O_2 and HF solution.[131] As shown in Fig. 24, four small rhombus {110} facets can be observed. As mentioned above, the {110} surface has the highest surface energy of low-index surfaces of anatase TiO_2 single crystals, and has under-coordinated 4c-Ti sites (two dangling bonds per Ti site). As a result, the synthesized anatase TiO_2 single crystals exhibited enhanced photocatalytic activities for degradation of methylene blue dye under ultraviolet light irradiation, in comparison with irregular TiO_2 product. It is worth noting that the percentage of highly reactive {110} facets on the synthesized TiO_2 is still very small due to the high surface energy, and increasing the percentage of {110} facets is therefore still a challenging issue.

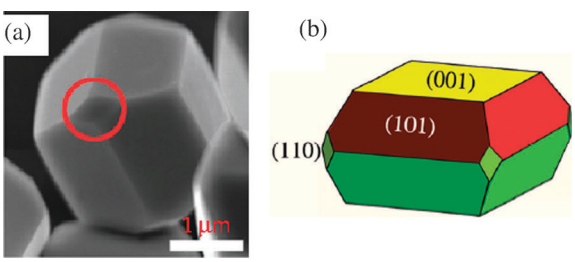

Fig. 24 (a) SEM image of anatase TiO_2 single crystals with square {001} and small rhombus {110} facets. (b) Schematic diagram of an anatase single crystal (modified with permission from ref. 131, copyright 2010, Royal Society of Chemistry).

4.2 SnO_2

Tin dioxide (SnO_2) has been widely used in photocatalysis, gas-sensing and also in rechargeable lithium batteries. The gas sensing of SnO_2 is based on the oxidation or reduction reaction of the detected gases occurring on its surfaces, which leads to an abrupt change in conductance. The gas-sensing ability of SnO_2 is therefore very sensitive to its surface structure. SnO_2 has the tetragonal rutile phase structure with lattice constants of a = 4.738 and c = 3.187. The surface energy of high-index planes of SnO_2 is also higher than that of low-index planes. For example, the {221} plane of SnO_2 have a relatively higher surface energy (2.28 J m^{-2}) than common low-index planes, such as {110} (1.401 J m^{-2}), {101} (1.554 J m^{-2}) and {100} (1.648 J m^{-2}), *i.e.*, $\gamma_{\{221\}} > \gamma_{\{100\}} > \gamma_{\{101\}} > \gamma_{\{110\}}$.[132]

Xie *et al.*[112] have synthesized octahedral SnO_2 nanocrystals with high-index {221} facets through a hydrothermal method with the assistance of HCl and PVP. By changing the amount of HCl to control the hydrolysis rate of $SnCl_4$ to form SnO_2 and the specific adsorption of Cl^- ions on SnO_2 surfaces, the morphologies of the obtained SnO_2 can be varied from octahedrons (nearly 100% of high-energy {221} facets) to elongated octahedrons, and finally to lance-like nanorods (Fig. 25a–c). The elongated octahedral SnO_2 are bounded by low-energy {110} facets in the middle parts and high-energy {221} facets (56%) at the pyramidal tips. As for the lance-like SnO_2 nanorods, the dominant facets are low-energy {110}, and the percentage of high-energy {221} facets is only about 13%.

For rutile SnO_2, Sn atoms in the bulk are sixfold-coordinated by O atoms. As shown in Fig. 25d, on the (110) surface, there are sixfold-coordinated Sn atoms (blue) and fivefold-coordinated Sn atoms (yellow) with one dangling bond. On the (221) surface, however, all Sn atoms are coordinatively unsaturated, located in fivefold-coordinated sites (yellow) and fourfold-coordinated sites (green) with two dangling bonds.

Since the {221} surface has a high density of dangling bonds, the {221}-exposed octahedral SnO_2 nanocrystals are anticipated to show good performance in gas sensing. Fig. 25e demonstrates sensing sensitivity curves of the three kinds of SnO_2 particles as a function of ethanol concentration. As expected, the sensitivity of the octahedral SnO_2 particles is much higher than those of the other two SnO_2 samples. Further analysis indicates that the sensing activity is proportional to the percentage of {221} facets among the exposed surfaces.

4.3 Lithium Mn-rich metal oxides for lithium ion batteries

The increasing demand for batteries of high power and high energy density, especially for use in electric vehicles, has stimulated great research interest focusing on lithium ion batteries. It is believed that the high power is related with rate-capability, *i.e.* storage of electrical energy at high charge and discharge rate. The structure of electrode materials, especially the surface structure, is a crucial factor that determines the rate for Li ion insertion/extraction, as this process might be a crystal face-sensitive process.

It is evidenced that Li ion can only insert into the bulk of a crystal in open structure planes of electrode materials, such as the (010) plane of a α-$NaFeO_2$ structured transition oxide materials and olivine structured $LiFePO_4$,[15,133–135] as well as the (001) plane of anatase TiO_2.[136,137] However, the synthesis of oxide nanomaterials with open surface structures is a well-known challenge, due to their high surface energy.

Lithium Mn-rich metal oxides such as $Li[Li_{1/3-2x/3}M_xMn_{2/3-x/3}]O_2$ (M = Ni, Co, Cr) are currently receiving significant attention for use as cathode materials for next-generation LIBs, owing to their high capacity of over 200 mA h g^{-1}. However, the low rate-capability of this kind of material prevents its use as a cathode material in dynamic

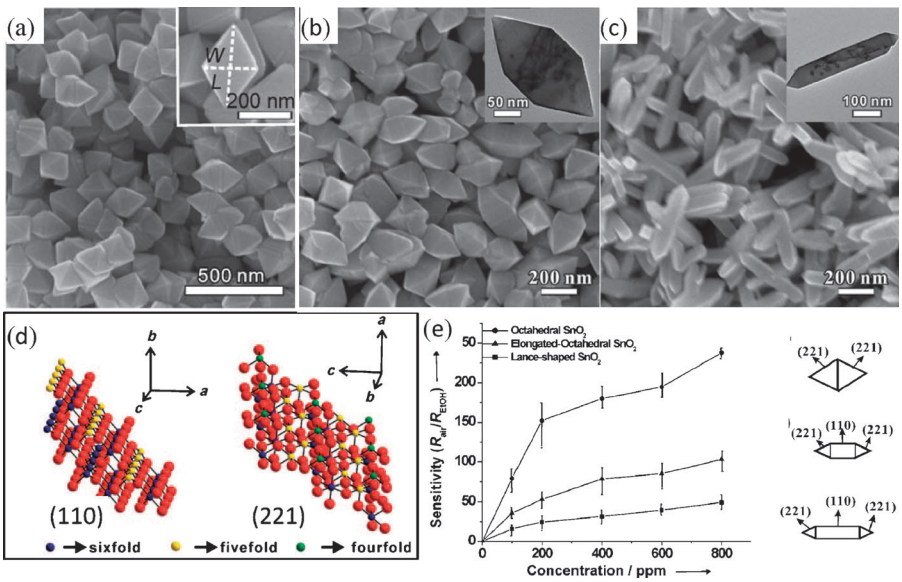

Fig. 25 SEM images of SnO_2 nanocrystals with different shapes: (a) octahedra with {221} facets; (b) elongated octahedra with {221} and {110} facets and (c) lance-like nanorods with {221} and {110} facets. (d) Schematic models of (110) and (221) on SnO_2. (e) Sensitivity curves of SnO_2 nanocrystals with different shapes as a function of ethanol concentration (modified with permission from ref. 112, copyright 2009, Wiley-VCH).

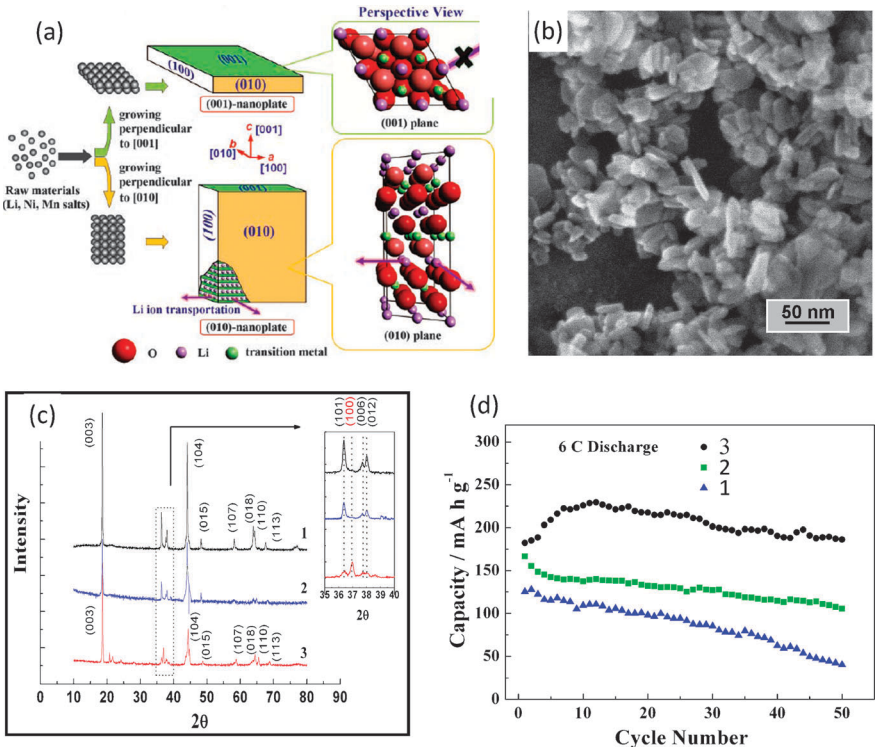

Fig. 26 (a) Schematic illustration of two kinds of nanoplates and the microstructure of their surfaces. (b) SEM characterization of the crystal habit-tuned LNMO. (c, d) XRD patterns and discharge capacity at a 6C rate of (1) LNMO particles, (2) conversional nanoplate-LNMO and (3) crystal habit-tuned nanoplate-LNMO (modified with permission from ref. 15, copyright 2010, Wiley-VCH).

lithium ion batteries for electric vehicle application. Extensive efforts have been made to improve the rate-capability and cycleability of this material by the synthesis of nanostructured $Li[Li_{1/3-2x/3}M_xMn_{2/3-x/3}]O_2$, which possesses a short Li ion transportation path due to the reduced dimensions. In a routine synthesis process, the (001) faceted nanomaterials are thermodynamic equilibrium products as the (001) plane presents a lower surface energy than the (010) plane. Due to lower electrochemical activity of the (001) plane for Li ion intercalation, the nanoplate's rate-performance was always poor (Fig. 26a). Recently a crystal habit-tuned nanoplate material of $Li(Li_{0.17}Ni_{0.25}Mn_{0.58})O_2$ (LNMO) has been successfully synthesized by Wei and co-workers, in which the proportion of the high energy (010) facets has been significantly increased in comparison with the conventional thermodynamic equilibrium nanoplate material (Fig. 26b and c).[15] In this synthesis route, a novel precursor and the short time of hydrothermal conditions led to the nanoplate growing simultaneously in the [010] direction, which increases the yield of (010) facet dominant nanoplates. This habit-tuned LNMO nanoplate material exhibits not only a high reversible capacity but also an excellent cycleability. At a 6C rate of charge/discharge, the reversible capacity measured at 50th cycle reaches 186 mA h g^{-1} (Fig. 26d). In comparison with 106 mA h g^{-1} for a conventional LNMO nanoplate and 40 mA h g^{-1} for LNMO particle materials measured at the 50th cycle under the same rate of charge/discharge, the rate capability of the habit-tuned LNMO nanoplate has been enhanced 1.75 and 4.65 times, respectively. The excellent high-rate performance has been attributed to the increased active surface area for Li ion intercalation/deintercalation on the (010) facet dominant nanomaterials. This study demonstrated that the proportion of electrochemically active surface for Li ion transportation is extensively increased by the increase of crystal planes of high surface energy and open surface structure. Recently, Wang *et al.* also reported that Li-intercalation/deintercalation dynamics is sensitive to the surface structure of $LiCoO_2$ oxide nanomaterials.[138]

Anatase titanium dioxide (TiO_2) with a tetragonal crystal structure has been intensively investigated as an electrode material for lithium-ion batteries because of its low cost, high stability, abundance and non-toxicity. As mentioned above, the (001) plane on anatase TiO_2 presents an open surface structure, whose surface energy is higher than the (101) plane. By comparison of the performance of anatase TiO_2 oxide nanomaterials with different percentages of (001/101) planes, an enhanced lithium ion insertion/extraction behavior for anatase TiO_2 oxide nanomaterials with dominant (001) surfaces has been demonstrated. The enhanced performance of the (001) dominated oxide nanomaterials is ascribed to a lower energy barrier for surface migration of Li ions across the (001) facet.[125,139] Recently, Lou and co-workers have reported a synthesis of hierarchical spheres self-organized from ultra-thin anatase TiO_2 nanosheets with nearly 100% exposed (001) facets. When it was charged at a rate of 1 C, a reversible capacity of 174 mA h g^{-1} was retained after more than 100 cycles (Fig. 27).[125]

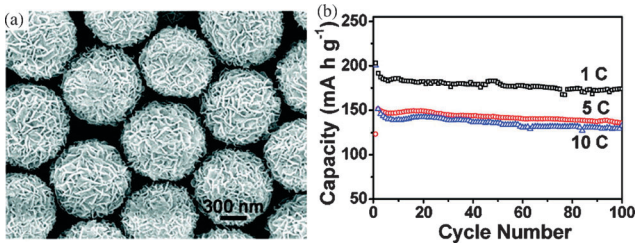

Fig. 27 (a) SEM images and (b) cycling performance at different rates of hierarchical spheres self-organized from ultrathin anatase TiO_2 nanosheets with {001} facets (modified with permission from ref. 125, copyright 2009, American Chemical Society).

5. Conclusion

Surface structure is the key to manipulating the physicochemical properties of nanomaterials. This review puts emphasis on the synthesis of metal and metal oxide nanomaterials with high surface energy and open surface structure. Greater control of crystal growth at the atomic scale is allowing scientists to realize the age-old-dream of designing nano-catalysts with high specificity and selectivity which someday could be designed to order. Nanomaterials with high surface energy, which possess a high density of reactive surface sites, have already been shown to exhibit exceptionally high electrocatalytic activity, as shown by crystals of Pt, Pd, Au and Fe and also high photocatalytic activity on metal oxide TiO_2. While the exceptional properties of these materials have been mostly demonstrated in the lab, it has not yet led to a revolution on the industrial scale, and few materials have seen significant widespread adoption. {221}-Exposed octahedral SnO_2 nanomaterials are particularly sensitive to ethanol gas, and have found their place in analytical applications while habit-tuned $Li(Li_{0.17}Ni_{0.25}Mn_{0.58})O_2$ (LNMO) nanoplates, dominated by high energy (010) surfaces, is a promising high rate-capability electrode material for use in dynamic lithium ion batteries. What currently restricts industrial use of these nanomaterials is our inability to fabricate them efficiently in high volume. A key issue is to develop unconventional electrochemical and wet chemistry methods that can alter the order of surface energy or stability of pristine high energy surfaces. This is an important emerging direction which underpins all high surface energy nanomaterial research. It is crucial, from the point of view of practical applications, to innovate synthesis technologies that enable size control (especially decreasing the size comparable to that of commercial catalysts) and mass production.

Other prospective research directions can be predicted as follows:

(1) Extending to other metal (Rh, Ru, Ni, Cu, *etc.*), alloys and oxide nanomaterials of high surface energy.

(2) Systematically tuning the surface structures of nanocrystal catalysts with high surface energy. As shown in Fig. 1 and 2, high-energy (or high-index) surfaces are variable.

(3) Surface modification by foreign atoms or compounds to change properties in relation to surface structure and electronic structure effects.

(4) Theoretical investigations of nanocrystals of high surface energy by density functional theory (DFT) calculations and molecular dynamics (MD) simulations, to reveal growth mechanisms (*e.g.*, the exact roles played by adsorbed oxygen atoms, surfactants and other additives), surface stability and surface reaction processes. Modeling investigations allow the prediction of new nanocrystal shapes with exceptional properties and help material scientists know what structures to look for. As new modeling techniques become available, new insights can be obtained for old systems.

(5) Exploring synthetic routes to large-scale production and possible applications of nanomaterials of high surface energy.

What is noteworthy is that remarkable progress has been made in wet chemical synthesis of high energy faceted metal nanocrystals. However, size control, especially synthesis of nanocrystals of high surface energy of several nanometres, is still a great challenge. The study of nanomaterials of high surface energy has already opened a new exciting avenue to design nanomaterials with exceptional properties for use in fuel cells, automotive catalytic converters, ammonia synthesis, photocatalysis and high performance materials for energy conversion and storage (*e.g.*, solar cells, lithium ion batteries).

Acknowledgements

This study was supported by Natural Science Foundation of China (20833005, 20873113, 20933004, 20921120405, 21073152 and 21021002), Major State Basic Research Development Program of China (2009CB220102) and the Fundamental Research Funds for the Central Universities (2010121021). Dr Ian Broadwell also wishes to express thanks to the EU Science and Technology Fellowship Program (EuropeAid/127024/L/ACT/CN_STF/11) along with the Chinese Postdoctoral Science Foundation (20100480715) for supporting his stay in Xiamen University.

References

1 C. Burda, X. B. Chen, R. Narayanan and M. A. El-Sayed, *Chem. Rev.*, 2005, **105**, 1025.
2 M. Haruta, *CATTECH*, 2002, **6**, 102.
3 D. Astruc, F. Lu and J. R. Aranzaes, *Angew. Chem., Int. Ed.*, 2005, **44**, 7852.
4 M. C. Daniel and D. Astruc, *Chem. Rev.*, 2004, **104**, 293.
5 G. A. Somorjai, *Science*, 1978, **201**, 489.
6 F. Tao and M. Salmeron, *Science*, 2011, **331**, 171.
7 D. L. Feldheim, *Science*, 2007, **316**, 699.
8 Z. L. Wang, *J. Phys. Chem. B*, 2000, **104**, 1153.
9 Y. N. Wen and H. M. Zhang, *Solid State Commun.*, 2007, **144**, 163.
10 N. P. Lebedeva, M. T. M. Koper, J. M. Feliu and R. A. van Santen, *J. Phys. Chem. B*, 2002, **106**, 12938.
11 S. L. Bernasek and G. A. Somorjai, *Surf. Sci.*, 1975, **48**, 204.
12 S. G. Sun, A. C. Chen, T. S. Huang, J. B. Li and Z. W. Tian, *J. Electroanal. Chem.*, 1992, **340**, 213.
13 R. A. Van Santen, *Acc. Chem. Res.*, 2009, **42**, 57.
14 N. Tian, Z. Y. Zhou and S. G. Sun, *J. Phys. Chem. C*, 2008, **112**, 19801.
15 G. Z. Wei, X. Lu, F. S. Ke, L. Huang, J. T. Li, Z. X. Wang, Z. Y. Zhou and S. G. Sun, *Adv. Mater.*, 2010, **22**, 4364.
16 H. E. Buckley, *Crystal Growth*, Wiley, New York, 1951.
17 T. S. Ahmadi, Z. L. Wang, T. G. Green, A. Henglein and M. A. El-Sayed, *Science*, 1996, **272**, 1924.
18 C. K. Tsung, J. N. Kuhn, W. Y. Huang, C. Aliaga, L. I. Hung, G. A. Somorjai and P. D. Yang, *J. Am. Chem. Soc.*, 2009, **131**, 5816.
19 J. T. Ren and R. D. Tilley, *J. Am. Chem. Soc.*, 2007, **129**, 3287.

20 C. Wang, H. Daimon, Y. Lee, J. Kim and S. Sun, *J. Am. Chem. Soc.*, 2007, **129**, 6974.
21 H. Lee, S. E. Habas, S. Kweskin, D. Butcher, G. A. Somorjai and P. D. Yang, *Angew. Chem., Int. Ed.*, 2006, **45**, 7824.
22 Y. T. Yu and B. Q. Xu, *Appl. Organomet. Chem.*, 2006, **20**, 638.
23 H. Song, F. Kim, S. Connor, G. A. Somorjai and P. D. Yang, *J. Phys. Chem. B*, 2005, **109**, 188.
24 X. Y. Fu, Y. A. Wang, N. Z. Wu, L. L. Gui and Y. Q. Tang, *Langmuir*, 2002, **18**, 4619.
25 S. Y. Zhao, S. H. Chen, S. Y. Wang, D. G. Li and H. Y. Ma, *Langmuir*, 2002, **18**, 3315.
26 A. Miyazaki and Y. Nakano, *Langmuir*, 2000, **16**, 7109.
27 A. C. Chen and P. Holt-Hindle, *Chem. Rev.*, 2010, **110**, 3767.
28 Z. M. Peng and H. Yang, *Nano Today*, 2009, **4**, 143.
29 J. Y. Chen, B. Lim, E. P. Lee and Y. N. Xia, *Nano Today*, 2009, **4**, 81.
30 N. Tian, Z. Y. Zhou, S. G. Sun, Y. Ding and Z. L. Wang, *Science*, 2007, **316**, 732.
31 H. G. Yang, C. H. Sun, S. Z. Qiao, J. Zou, G. Liu, S. C. Smith, H. M. Cheng and G. Q. Lu, *Nature*, 2008, **453**, 638.
32 Z. Y. Jiang, Q. Kuang, Z. X. Xie and L. S. Zheng, *Adv. Funct. Mater.*, 2010, **20**, 3634.
33 A. R. Tao, S. Habas and P. D. Yang, *Small*, 2008, **4**, 310.
34 Y. Xia, Y. J. Xiong, B. Lim and S. E. Skrabalak, *Angew. Chem., Int. Ed.*, 2009, **48**, 60.
35 J. F. Nicholas, *An Atlas of Models of Crystal Surfaces*, Gordon & Breach, New York, 1965.
36 A. A. Proussevitch and D. L. Sahagian, *Comput. Geosci.*, 2001, **27**, 441.
37 A. T. Bell, *Science*, 2003, **299**, 1688.
38 F. Zaera, *Appl. Catal., A*, 2002, **229**, 75.
39 J. Larminie and A. Dicks, *Fuel Cell Systems Explained*, John Wiley & Sons Chichester, West Sussex, UK, 2nd edn, 2003.
40 R. M. Heck and R. J. Farrauto, *Appl. Catal., A*, 2001, **221**, 443.
41 Q. Cheng, Y. X. Jiang, N. Tian, Z. Y. Zhou and S. G. Sun, *Electrochim. Acta*, 2010, **55**, 8273.
42 F. Ma, S. L. Ma, K. W. Xu and P. K. Chu, *J. Phys. Chem. C*, 2008, **112**, 3247.
43 Y. H. Wen, H. Fang, Z. Z. Zhu and S. G. Sun, *Chem. Phys. Lett.*, 2009, **471**, 295.
44 A. Visintin, J. C. Canullo, W. E. Triaca and A. J. Arvia, *J. Electroanal. Chem.*, 1988, **239**, 67.
45 J. Clavilier, R. Durand, G. Guinet and R. Faure, *J. Electroanal. Chem.*, 1981, **127**, 281.
46 J. Clavilier, D. Armand, S. G. Sun and M. Petit, *J. Electroanal. Chem.*, 1986, **205**, 267.
47 J. Clavilier, R. Faure, G. Guinet and R. Durand, *J. Electroanal. Chem.*, 1979, **107**, 205.
48 N. Furuya and M. Shibata, *J. Electroanal. Chem.*, 1999, **467**, 85.
49 Z. Nagy and H. You, *Electrochim. Acta*, 2002, **47**, 3037.
50 Y. H. Fang and Z. P. Liu, *J. Phys. Chem. C*, 2009, **113**, 9765.
51 B. C. Han, C. R. Miranda and G. Ceder, *Phys. Rev. B: Condens. Matter Mater. Phys.*, 2008, **77**, 075410.
52 Z. Y. Zhou, N. Tian, Z. Z. Huang, D. J. Chen and S. G. Sun, *Faraday Discuss.*, 2009, **140**, 81.
53 Y. J. Xiong, J. M. McLellan, Y. D. Yin and Y. N. Xia, *Angew. Chem., Int. Ed.*, 2007, **46**, 790.
54 Y. G. Sun, B. Mayers, T. Herricks and Y. N. Xia, *Nano Lett.*, 2003, **3**, 955.
55 S. H. Zhang, Z. Y. Jiang, Z. X. Xie, X. Xu, R. B. Huang and L. S. Zheng, *J. Phys. Chem. B*, 2005, **109**, 9416.
56 I. Lisiecki, A. Filankembo, H. Sack-Kongehl, K. Weiss, M. P. Pileni and J. Urban, *Phys. Rev. B: Condens. Matter*, 2000, **61**, 4968.
57 C. Lofton and W. Sigmund, *Adv. Funct. Mater.*, 2005, **15**, 1197.
58 H. S. Liu, C. J. Song, L. Zhang, J. J. Zhang, H. J. Wang and D. P. Wilkinson, *J. Power Sources*, 2006, **155**, 95.
59 R. Borup, J. Meyers, B. Pivovar, Y. S. Kim, R. Mukundan, N. Garland, D. Myers, M. Wilson, F. Garzon, D. Wood, P. Zelenay, K. More, K. Stroh, T. Zawodzinski, J. Boncella, J. E. McGrath, M. Inaba, K. Miyatake, M. Hori, K. Ota, Z. Ogumi, S. Miyata, A. Nishikata, Z. Siroma, Y. Uchimoto, K. Yasuda, K. I. Kimijima and N. Iwashita, *Chem. Rev.*, 2007, **107**, 3904.
60 Z. Y. Zhou, Z. Z. Huang, D. J. Chen, Q. Wang, N. Tian and S. G. Sun, *Angew. Chem., Int. Ed.*, 2010, **49**, 411.
61 Y. H. Wen, H. Fang, Z. Z. Zhu and S. G. Sun, *Phys. Lett. A*, 2009, **373**, 272.
62 T. Yu, D. Y. Kim, H. Zhang and Y. N. Xia, *Angew. Chem., Int. Ed.*, 2011, **50**, 2773.
63 H. Zhang, W. Y. Li, M. S. Jin, J. Zeng, T. Yu, D. Yang and Y. N. Xia, *Nano Lett.*, 2011, **11**, 898.
64 Y. J. Li and Y. Huang, *Adv. Mater.*, 2010, **22**, 1921.
65 W. P. Zhou, A. Lewera, R. Larsen, R. I. Masel, P. S. Bagus and A. Wieckowski, *J. Phys. Chem. B*, 2006, **110**, 13393.
66 C. W. Xu, H. Wang, P. K. Shen and S. P. Jiang, *Adv. Mater.*, 2007, **19**, 4256.
67 H. S. Gandhi, G. W. Graham and R. W. McCabe, *J. Catal.*, 2003, **216**, 433.
68 R. Narayanan and M. A. El-Sayed, *J. Am. Chem. Soc.*, 2003, **125**, 8340.
69 J. Y. Wang, Y. Y. Kang, H. Yang and W. B. Cai, *J. Phys. Chem. C*, 2009, **113**, 8366.
70 N. Tian, Z. Y. Zhou, N. F. Yu, L. Y. Wang and S. G. Sun, *J. Am. Chem. Soc.*, 2010, **132**, 7580.
71 N. Tian, Z. Y. Zhou and S. G. Sun, *Chem. Commun.*, 2009, 1502.
72 Y. J. Xiong, H. G. Cai, B. J. Wiley, J. G. Wang, M. J. Kim and Y. N. Xia, *J. Am. Chem. Soc.*, 2007, **129**, 3665.
73 X. Q. Huang, S. H. Tang, H. H. Zhang, Z. Y. Zhou and N. F. Zheng, *J. Am. Chem. Soc.*, 2009, **131**, 13916.
74 L. Xiao, L. Zhuang, Y. Liu, J. T. Lu and H. D. Abruna, *J. Am. Chem. Soc.*, 2009, **131**, 602.
75 W. X. Niu, L. Zhang and G. B. Xu, *ACS Nano*, 2010, **4**, 1987.
76 J. Watt, N. Young, S. Haigh, A. Kirkland and R. D. Tilley, *Adv. Mater.*, 2009, **21**, 2288.
77 J. Watt, S. Cheong, M. F. Toney, B. Ingham, J. Cookson, P. T. Bishop and R. D. Tilley, *ACS Nano*, 2010, **4**, 396.
78 S. Patra, B. Viswanath, K. Barai, N. Ravishankar and N. Munichandraiah, *ACS Appl. Mater. Interfaces*, 2010, **2**, 2965.
79 Y. X. Fang, S. J. Guo, C. Z. Zhu, S. J. Dong and E. K. Wang, *Langmuir*, 2010, **26**, 17816.
80 C. L. Lu, K. S. Prasad, H. L. Wu, J. A. Ho and M. H. Huang, *J. Am. Chem. Soc.*, 2010, **132**, 14546.
81 Y. Yu, Q. B. Zhang, B. Liu and J. Y. Lee, *J. Am. Chem. Soc.*, 2010, **132**, 18258.
82 F. Wang, C. H. Li, L. D. Sun, H. S. Wu, T. Ming, J. F. Wang, J. C. Yu and C. H. Yan, *J. Am. Chem. Soc.*, 2011, **133**, 1106.
83 M. Haruta, N. Yamada, T. Kobayashi and S. Iijima, *J. Catal.*, 1989, **115**, 301.
84 Y. Y. Yu, S. S. Chang, C. L. Lee and C. R. C. Wang, *J. Phys. Chem. B*, 1997, **101**, 6661.
85 Z. L. Wang, M. B. Mohamed, S. Link and M. A. El-Sayed, *Surf. Sci.*, 1999, **440**, L809.
86 M. Z. Liu and P. Guyot-Sionnest, *J. Phys. Chem. B*, 2005, **109**, 22192.
87 Y. Chen, C. Somsen, S. Milenkovic and A. W. Hassel, *J. Mater. Chem.*, 2009, **19**, 924.
88 Y. Chen, S. Milenkovic and A. W. Hassel, *ChemPhysChem*, 2010, **11**, 2838.
89 H. G. Liao, Y. X. Jiang, Z. Y. Zhou, S. P. Chen and S. G. Sun, *Angew. Chem., Int. Ed.*, 2008, **47**, 9100.
90 Y. Y. Ma, Q. Kuang, Z. Y. Jiang, Z. X. Xie, R. B. Huang and L. S. Zheng, *Angew. Chem., Int. Ed.*, 2008, **47**, 8901.
91 Y. Yu, Q. B. Zhang, X. M. Lu and J. Y. Lee, *J. Phys. Chem. C*, 2010, **114**, 11119.
92 T. Ming, W. Feng, Q. Tang, F. Wang, L. D. Sun, J. F. Wang and C. H. Yan, *J. Am. Chem. Soc.*, 2009, **131**, 16350.
93 J. Li, L. H. Wang, L. Liu, L. Guo, X. D. Han and Z. Zhang, *Chem. Commun.*, 2010, **46**, 5109.
94 J. A. Zhang, M. R. Langille, M. L. Personick, K. Zhang, S. Y. Li and C. A. Mirkin, *J. Am. Chem. Soc.*, 2010, **132**, 14012.
95 D. Y. Kim, S. H. Im and O. O. Park, *Cryst. Growth Des.*, 2010, **10**, 3321.
96 T. T. Tran and X. Lu, *J. Phys. Chem. C*, 2011, **115**, 3638.
97 E. Carbo-Argibay, B. Rodriguez-Gonzalez, S. Gomez-Grana, A. Guerrero-Martinez, I. Pastoriza-Santos, J. Perez-Juste and L. M. Liz-Marzan, *Angew. Chem., Int. Ed.*, 2010, **49**, 9397.
98 W. X. Niu, S. L. Zheng, D. W. Wang, X. Q. Liu, H. J. Li, S. A. Han, J. Chen, Z. Y. Tang and G. B. Xu, *J. Am. Chem. Soc.*, 2009, **131**, 697.
99 G. H. Jeong, M. Kim, Y. W. Lee, W. Choi, W. T. Oh, Q. H. Park and S. W. Han, *J. Am. Chem. Soc.*, 2009, **131**, 1672.

100 D. Y. Kim, S. H. Im, O. O. Park and Y. T. Lim, *CrystEngComm*, 2010, **12**, 116.
101 X. G. Liu, N. Q. Wu, B. H. Wunsch, R. J. Barsotti and F. Stellacci, *Small*, 2006, **2**, 1046.
102 Y. Chen, X. Gu, C. G. Nie, Z. Y. Jiang, Z. X. Xie and C. J. Lin, *Chem. Commun*., 2005, 4181.
103 D. W. Wang, Y. Liu and T. Y. You, *CrystEngComm*, 2010, **12**, 4028.
104 N. D. Spencer, R. C. Schoonmaker and G. A. Somorjai, *Nature*, 1981, **294**, 643.
105 Y. X. Chen, S. P. Chen, Z. Y. Zhou, N. Tian, Y. X. Jiang, S. G. Sun, Y. Ding and Z. L. Wang, *J. Am. Chem. Soc*., 2009, **131**, 10860.
106 Y. X. Chen, S. P. Chen, Q. S. Chen, Z. Y. Zhou and S. G. Sun, *Electrochim. Acta*, 2008, **53**, 6938.
107 N. A. Pangarov, *J. Electroanal. Chem*., 1965, **9**, 70.
108 Y. Q. Dai, C. M. Cobley, J. Zeng, Y. M. Sun and Y. N. Xia, *Nano Lett*., 2009, **9**, 2455.
109 X. G. Han, Q. Kuang, M. S. Jin, Z. X. Xie and L. S. Zheng, *J. Am. Chem. Soc*., 2009, **131**, 3152.
110 B. H. Wu, C. Y. Guo, N. F. Zheng, Z. X. Xie and G. D. Stucky, *J. Am. Chem. Soc*., 2008, **130**, 17563.
111 G. Liu, H. G. Yang, X. W. Wang, L. N. Cheng, H. F. Lu, L. Z. Wang, G. Q. Lu and H. M. Cheng, *J. Phys. Chem. C*, 2009, **113**, 21784.
112 X. G. Han, M. S. Jin, S. F. Xie, Q. Kuang, Z. Y. Jiang, Y. Q. Jiang, Z. X. Xie and L. S. Zheng, *Angew. Chem., Int. Ed*., 2009, **48**, 9180.
113 X. Zhou, Z. X. Xie, Z. Y. Jiang, Q. Kuang, S. H. Zhang, T. Xu, R. B. Huang and L. S. Zheng, *Chem. Commun*., 2005, 5572.
114 T. Xu, X. Zhou, Z. Y. Jiang, Q. Kuang, Z. X. Xie and L. S. Zheng, *Cryst. Growth Des*., 2009, **9**, 192.
115 M. Leng, M. Z. Liu, Y. B. Zhang, Z. Q. Wang, C. Yu, X. G. Yang, H. J. Zhang and C. Wang, *J. Am. Chem. Soc*., 2010, **132**, 17084.
116 J. Z. Yin, Z. N. Yu, F. Gao, J. J. Wang, H.A. Pang and Q. Y. Lu, *Angew. Chem., Int. Ed*., 2010, **49**, 6328.
117 B. Y. Geng, J. Z. Ma and J. H. You, *Cryst. Growth Des*., 2008, **8**, 1443.
118 S. H. Liu, F. Lu, R. M. Xing and J. J. Zhu, *Chem.–Eur. J*., 2011, **17**, 620.
119 M. S. Wang and Q. W. Chen, *Chem.–Eur. J*., 2010, **16**, 12088.
120 D. B. Fan, P. J. Thomas and P. O'Brien, *J. Am. Chem. Soc*., 2008, **130**, 10892.
121 M. Lazzeri, A. Vittadini and A. Selloni, *Phys. Rev. B: Condens. Matter*, 2001, **63**, 155409.
122 M. Lazzeri, A. Vittadini and A. Selloni, *Phys. Rev. B: Condens. Matter*, 2002, **65**, 119901.
123 H. G. Yang, G. Liu, S. Z. Qiao, C. H. Sun, Y. G. Jin, S. C. Smith, J. Zou, H. M. Cheng and G. Q. Lu, *J. Am. Chem. Soc*., 2009, **131**, 4078.
124 J. F. Porter, Y. G. Li and C. K. Chan, *J. Mater. Sci*., 1999, **34**, 1523.
125 J. S. Chen, Y. L. Tan, C. M. Li, Y. L. Cheah, D. Y. Luan, S. Madhavi, F. Y. C. Boey, L. A. Archer and X. W. Lou, *J. Am. Chem. Soc*., 2010, **132**, 6124.
126 J. M. Li and D. S. Xu, *Chem. Commun*., 2010, **46**, 2301.
127 Z. K. Zheng, B. B. Huang, X. Y. Qin, X. Y. Zhang, Y. Dai, M. H. Jiang, P. Wang and M. H. Whangbo, *Chem.–Eur. J*., 2009, **15**, 12576.
128 S. W. Liu, J. G. Yu and M. Jaroniec, *J. Am. Chem. Soc*., 2010, **132**, 11914.
129 M. Liu, L. Y. Piao, W. M. Lu, S. T. Ju, L. Zhao, C. L. Zhou, H. L. Li and W. J. Wang, *Nanoscale*, 2010, **2**, 1115.
130 H. M. Zhang, Y. H. Han, X. L. Liu, P. R. Liu, H. Yu, S. Q. Zhang, X. D. Yao and H. J. Zhao, *Chem. Commun*., 2010, **46**, 8395.
131 M. Liu, L. Y. Piao, L. Zhao, S. T. Ju, Z. J. Yan, T. He, C. L. Zhou and W. J. Wang, *Chem. Commun*., 2010, **46**, 1664.
132 B. Slater, C. R. A. Catlow, D. H. Gay, D. E. Williams and V. Dusastre, *J. Phys. Chem. B*, 1999, **103**, 10644.
133 B. Kang and G. Ceder, *Nature*, 2009, **458**, 190.
134 M. S. Islam, D. J. Driscoll, C. A. J. Fisher and P. R. Slater, *Chem. Mater*., 2005, **17**, 5085.
135 D. Morgan, A. Van der Ven and G. Ceder, *Electrochem. Solid-State Lett*., 2004, **7**, A30.
136 G. Y. Chen, X. Y. Song and T. J. Richardson, *Electrochem. Solid-State Lett*., 2006, **9**, A295.
137 C. H. Sun, X. H. Yang, J. S. Chen, Z. Li, X. W. Lou, C. Z. Li, S. C. Smith, G. Q. Lu and H. G. Yang, *Chem. Commun*., 2010, **46**, 6129.
138 D. S. Wang, X. L. Ma, Y. G. Wang, L. Wang, Z. Y. Wang, W. Zheng, X. M. He, J. Li, Q. Peng and Y. D. Li, *Nano Res*., 2010, **3**, 1.
139 M. Bousa, B. Laskova, M. Zukalova, J. Prochazka, A. Chou and L. Kavan, *J. Electrochem. Soc*., 2010, **157**, A1108.